Comput. Methods Appl. Mech. Engrg. 200 (2011) 2577–2593

Contents lists available at ScienceDirect

Comput. Methods Appl. Mech. Engrg.

journal homepage: www.elsevier.com/locate/cma

A variational multiscale method for incompressible turbulent flows: Bubble functions and fine scale fields

Arif Masud *, Ramon Calderer

Department of Civil and Environmental Engineering, University of Illinois at Urbana-Champaign, 205 North Mathews Avenue, Urbana, IL 61801, USA

ARTICLE INFO

Article history:
Received 25 October 2010
Received in revised form 18 February 2011
Accepted 8 April 2011
Available online 22 April 2011

Keywords:
Residual-based turbulence model
Variational multiscale method
Large eddy simulation
Stabilized finite elements
Turbulence modeling
Bubble functions

ABSTRACT

This paper presents a residual-based turbulence model for the incompressible Navier–Stokes equations. The method is derived employing the variational multiscale (VMS) framework. A multiscale decomposition of the continuous solution and a priori unique decomposition of the admissible spaces of functions lead to two coupled nonlinear problems termed as the coarse-scale and the fine-scale sub-problems. The fine-scale velocity field is assumed to be nonlinear and time-dependent and is modeled via the bubble functions approach applied directly to the fine-scale sub-problem. A significant contribution in this paper is a systematic and consistent derivation of the fine-scale variational operator, commonly termed as the stabilization tensor that possesses the right order in the advective and diffusive limits, and variationally projects the fine-scale solution onto the coarse-scale space. A direct treatment of the fine-scale problem via bubble functions offers several fine-scale approximation options with varying degrees of mathematical sophistication that are investigated via benchmark problems. Numerical accuracy of the proposed method is shown on a forced-isotropic turbulence problem, statistically stationary turbulent channel flow problems at $Re_\tau = 395$ and 590, and non-equilibrium turbulent flow around a cylinder at $Re = 3{,}900$.

1. Introduction

Large eddy simulation (LES) provides computationally economic solutions to the modeling of turbulence as compared to the direct numerical simulation (DNS) wherein all the scales of turbulence are numerically resolved. Several techniques have been adopted under the traditional LES framework to model the small scale effects in the turbulent flow regime and reasonable success has been achieved for various geometric configurations and Reynolds numbers. Most of the traditional LES techniques emphasize the use of eddy viscosity models such as the constant-coefficient Smagorinsky-type models [48] and the dynamic viscosity models [14,31]. Nevertheless, LES models that are not based on viscosity models have also been proposed [2]. For a non-exhaustive collection of methods for LES modeling, the reader could refer to [48,2,14,31,10,26,40,32,42,49,50] and references therein.

In recent years new LES models that are based on the variational multiscale (VMS) framework proposed by Hughes et al. [22,23] have been presented. The first applications of the VMS method to the modeling of turbulence by Hughes et al. [24,25] were based on three-level scale decomposition involving coarse-, fine- and the modeled-scales. The early versions of VMS-based turbulence models employed both Smagorinsky-type constant-coefficient viscosities [48], as well as the dynamic viscosities [14,31], and good results were obtained for a variety of test cases. It was observed that within the VMS framework, the dynamic viscosity models yield superior results as compared to the static eddy viscosity models. Adopting VMS approach, three-scale turbulence models in the context of finite element methods were presented in [9,15,16], and in the context of finite volume methods on unstructured grids were presented by Farhat and co-workers [29,11,46,47].

Subsequent developments in VMS based turbulence models adopted a two-level scale separation [43,3,8,1,4,13,18]. The key idea underlying the VMS framework is *a priori* direct sum decomposition of the space of functions into coarse- and fine-scale space. This decoupling of the physical scales that is represented via the appropriate spaces of functions is linked to a decomposition of the computational scales into two overlapping components that are categorized as coarse-scales and fine-scales, respectively. Typically the coarse-scales are represented via the traditional finite element shape functions, while the fine-scales that lie in an infinite-dimensional space, are defined to be the remaining part of the solution. The decoupling of the spaces of functions leads to the decomposition of the original problem into two sub-problems, namely, the coarse-scale sub-problem and the fine-scale sub-problem. The modeling aspect in the method lies in extracting the fine-scale solution from the nonlinear fine-scale sub-problem. This

* Corresponding author. Tel.: +1 217 244 2832; fax: +1 217 265 8039.
E-mail address: amasud@illinois.edu (A. Masud).

0045-7825/$ - see front matter © 2011 Elsevier B.V. All rights reserved.
doi:10.1016/j.cma.2011.04.010

fine-scale solution is then variationally projected onto the coarse-scale space, leading to a formulation that is expressed entirely in terms of the coarse-scales. This contribution of the nonlinear fine-scales that leads to nonlinear stabilization is interpreted as a way to model the turbulence phenomena. Although the final formulation does not depend explicitly on the fine-scale fields, the effects of fine-scales are consistently represented via the additional residual based terms. The large scale features in the solution of the final form are computationally resolved, and this aspect of the VMS-based models shares common threads with the LES strategies.

In this paper we primarily focus our attention to the modeling of the nonlinear fine-scale problem. Since the fine-scale velocity lies in an infinite-dimensional space, as a consequence, the fine-scale problem cannot be exactly resolved. This requires modeling assumptions on the fine-scales to help reduce the dimensionality of the problem and to estimate the fine-scale features that can then be projected onto the coarse-scale space. We endeavor to extend our earlier work on the variational multiscale methods in the context of laminar flows [39,7] wherein fine-scale problem was expanded in terms of bubble functions, to residual based turbulence models. The use of bubble functions for the modeling of fine-scales was successfully applied by us in the derivation of stabilized formulations for a variety of mixed field problems [33–37,28]. In this paper we show that in the context of turbulent flows, the use of bubble functions for expanding fine-scales leads to various design options for the VMS based turbulence models. The effects of these options on the numerical solution of the coarse-scale problem are investigated in the numerical section.

The paper is organized as follows. In Section 2, the incompressible Navier–Stokes equations are presented. In Section 3, we present the derivation of the residual-based turbulence model, where the time-dependent aspects of the fine-scales are emphasized. In Section 4, the proposed method is studied numerically via three test cases with increasing degree of complexity in the flow physics. In Section 4.2, using the turbulent channel flow problem for two different *Re* flows, we investigate the computational attributes of the various modeling assumptions stipulated in Section 3. Specifically, we evaluate the effects of fine-scale pressure field that is represented via an element-wise continuity term. We study the effects of accounting for the orthogonality of the sub-grid scales to the coarse-scale space that leads to the annihilation of the sub-grid scale viscosity term, and compare it with the case when this condition is not imposed. An important aspect of the fine-scale modeling involved in the fine-scale problem is the consideration and numerical evaluation of the residual of the Euler–Lagrange equations of the coarse-scales. We investigate the influence of considering the mean value of the residual versus the full residual on the modeled fine-scale velocity field in an effort to develop a mathematically rigorous and computationally economical model. An important issue in the modeling of reactive turbulent flows is that of the time step size in the otherwise implicit time integration schemes. It is now well documented that if the step-size employed in implicit schemes is of the order of the step-size of its underlying explicit-in-time scheme, spurious oscillations can appear [17]. This aspect is attributed to the issue of the violation of the principle of causality. In Section 4.2.5 we show that if the time terms in the expansion of the fine-scale velocity field are fully accounted for in the fine-scale time integration, this issue can be adequately addressed. Conclusions are drawn in Section 5.

2. The incompressible Navier–Stokes equations

Let $\Omega \subset \mathbb{R}^{n_{sd}}$ be a connected, open, bounded region with piecewise smooth boundary Γ. The number of space dimensions, n_{sd}, is equal to 3. The time interval of interest is denoted $]0, T[$, with $T > 0$. The initial/boundary-value problem consists of solving the following set of equations for $\boldsymbol{v} : \Omega \times]0, T[\to \mathbb{R}^{n_{sd}}$, the velocity, and $p : \Omega \times]0, T[\to \mathbb{R}$, the kinematic pressure:

$$\frac{\partial \boldsymbol{v}}{\partial t} + \nabla \cdot (\boldsymbol{v} \otimes \boldsymbol{v}) - 2\nu \nabla \cdot \varepsilon(\boldsymbol{v}) + \nabla p = \boldsymbol{f} \quad \text{in } \Omega, \tag{1}$$

$$\nabla \cdot \boldsymbol{v} = 0 \quad \text{in } \Omega, \tag{2}$$

$$\boldsymbol{v} = \boldsymbol{g} \quad \text{on } \Gamma, \tag{3}$$

$$\boldsymbol{v}(\boldsymbol{x}, 0) = \boldsymbol{v}_0 \quad \text{on } \Omega, \tag{4}$$

where $\boldsymbol{f} : \Omega \times]0, T[\to \mathbb{R}^{n_{sd}}$ is the body force (per unit of mass), ν is the kinematic viscosity (assumed positive and constant), $\boldsymbol{v}_0$ is the initial condition for the velocity field, $\boldsymbol{g}$ represents the Dirichlet boundary conditions, and $\otimes$ denotes the tensor product. $\varepsilon(\boldsymbol{v})$ is the strain-rate tensor which is defined as $\varepsilon(\boldsymbol{v}) = \nabla^s \boldsymbol{v} = [\nabla \boldsymbol{v} + (\nabla \boldsymbol{v})^{\mathrm{T}}]/2$. Eq. (1) is the momentum balance equation; Eq. (2) is the incompressibility constraint; Eq. (3) is the Dirichlet boundary condition; and Eq. (4) is the initial condition.

Let $\boldsymbol{w}(\boldsymbol{x}) \in \boldsymbol{\mathcal{V}} = \left(H_0^1(\Omega)\right)^{n_{sd}}$ and $q(\boldsymbol{x}) \in \mathcal{Q} = C^0(\Omega) \cap L^2(\Omega)$ represent the weighting functions for the velocity and the pressure fields, respectively. The appropriate spaces of functions for the velocity and pressure trial solutions are the corresponding time-dependent spaces $\boldsymbol{\mathcal{S}}$ and $\mathcal{P}$ that satisfy the initial and boundary conditions *ab initio*. The standard weak form of the problem is: find $\boldsymbol{v}(\boldsymbol{x}, t) \in \boldsymbol{\mathcal{S}}$ and $p(\boldsymbol{x}, t) \in \mathcal{P}$ such that for all $\boldsymbol{w}(\boldsymbol{x}) \in \boldsymbol{\mathcal{V}}$ and $q(\boldsymbol{x}) \in \mathcal{Q}$:

$$\left(\boldsymbol{w}, \frac{\partial \boldsymbol{v}}{\partial t}\right) - (\nabla \boldsymbol{w}, \boldsymbol{v} \otimes \boldsymbol{v}) + (\nabla^s \boldsymbol{w}, 2\nu \nabla^s \boldsymbol{v}) - (\nabla \cdot \boldsymbol{w}, p) = (\boldsymbol{w}, \boldsymbol{f}), \tag{5}$$

$$(q, \nabla \cdot \boldsymbol{v}) = 0, \tag{6}$$

where $(\cdot, \cdot) = \int_\Omega (\cdot) d\Omega$ is the $L^2(\Omega)$-inner product. Eqs. (5) and (6) imply weak satisfaction of the momentum equations and the continuity equation, in addition to the initial condition.

Remark 1. For the derivation of the VMS method presented in Section 3, we consider only the Dirichlet boundary conditions.

3. The variational multiscale method

Let $\{\Omega^e\}_{e=1}^{n_{el}}$ be a partition of Ω such that $\bigcup_{e=1}^{n_{el}} \overline{\Omega^e} = \Omega$ and $\bigcap_{e=1}^{n_{el}} \overline{\Omega^e} = \emptyset$. Here n_{el} denotes the number of elements in the domain Ω. The boundaries of the elements Ω^e are Γ^e, $e = 1, 2, \ldots, n_{el}$. The variational multiscale method [22,23,38] consists of decomposing the velocity field and the weighting functions into coarse- and fine-scales. The coarse-scale field belongs to a finite dimensional space of functions, and is typically represented by finite element shape functions. The fine-scale field, also called sub-grid scale field, is the remaining part of the solution. Although the space of the fine-scale field is infinite dimensional, it will be approximated by a finite dimensional sub-space spanned by bubble functions and this will constitute the modeling part of the fine-scale problem.

We assume a unique additive decomposition of the velocity field into coarse, or resolvable scales $\bar{\boldsymbol{v}}$, and fine, or unresolvable scales $\boldsymbol{v}'$ that are also considered as the rapidly fluctuating part of $\boldsymbol{v}$:

$$\boldsymbol{v}(\boldsymbol{x}, t) = \underbrace{\bar{\boldsymbol{v}}(\boldsymbol{x}, t)}_{\text{coarse scale}} + \underbrace{\boldsymbol{v}'(\boldsymbol{x}, t)}_{\text{fine scale}}. \tag{7}$$

The coarse and fine-scale fields belong to spaces of functions that accommodate a direct sum decomposition into $\overline{\boldsymbol{\mathcal{S}}}$ and $\boldsymbol{\mathcal{S}}'$, respectively:

$$\boldsymbol{\mathcal{S}} = \overline{\boldsymbol{\mathcal{S}}} \oplus \boldsymbol{\mathcal{S}}' \quad \text{and} \quad \boldsymbol{\mathcal{S}}' = \boldsymbol{\mathcal{S}} \setminus \overline{\boldsymbol{\mathcal{S}}}, \tag{8}$$

where $\overline{\mathcal{S}}$ is a finite-dimensional space and is identified with the standard finite element space (defined in Section 2). The fine-scale space $\mathcal{S}'$ is infinite dimensional and therefore various characterizations of $\mathcal{S}'$ are possible for the approximation of the fine-scale velocity field $\boldsymbol{v}'$ (see, e.g., [22]).

Remark 2. In our previous works [39,7], the fine-scale component $\boldsymbol{v}'$ was assumed to be represented by piecewise polynomials of sufficiently high order, continuous in space but piecewise constant-in-time. In this paper we relax the later assumption and allow the fine scales to continuously evolve in time.

Remark 3. Time dependent fine-scales are important to resolve some issues that appear when very small time step sizes are employed. For example, in residual-based turbulence models, for the case of quasi-static fine-scales, the fine-scale velocity field vanishes as the size of the time step approaches zero. Also the time dependent fine-scales are important to resolve the issues that are encountered when a very small step-size is employed in implicit time integration methods [17]. Residual-based turbulence models that account for the time-dependence of fine-scales have also been proposed in [13,18].

Likewise, we assume an overlapping sum decomposition of the weighting functions into coarse and fine-scale components denoted by $\bar{\boldsymbol{w}}$ and $\boldsymbol{w}'$, respectively:

$$\boldsymbol{w}(\boldsymbol{x}) = \underbrace{\bar{\boldsymbol{w}}(\boldsymbol{x})}_{\text{coarse scale}} + \underbrace{\boldsymbol{w}'(\boldsymbol{x})}_{\text{fine scale}}, \tag{9}$$

where $\bar{\boldsymbol{w}}(\boldsymbol{x})$ and $\boldsymbol{w}'(\boldsymbol{x})$ belong to the spaces of functions that accommodate a unique additive decomposition, i.e., $\mathcal{V} = \bar{\mathcal{V}} \oplus \mathcal{V}'$ and $\mathcal{V}' = \mathcal{V} \setminus \bar{\mathcal{V}}$. At this point, we make a simplifying assumption on the fine scales that although they are non-zero within the elements, they vanish identically over the element boundaries:

$$\boldsymbol{v}' = \boldsymbol{w}' = 0 \quad \text{on } \Gamma', \tag{10}$$

Remark 4. Eq. (10) is not a limitation of the method and it can be relaxed via Lagrange multiplier enforcement of the inter-element continuity of fine-scales.

Expressions (7) and (9) are substituted in the weak problem (5,6). Assuming that the spaces of coarse- and fine-scales are linearly independent as stipulated in Eq. (8), the two sub-problems become:

Coarse-scale sub-problem:

$$\left(\bar{\boldsymbol{w}}, \frac{\partial(\bar{\boldsymbol{v}} + \boldsymbol{v}')}{\partial t}\right) - (\nabla\bar{\boldsymbol{w}}, (\bar{\boldsymbol{v}} + \boldsymbol{v}') \otimes (\bar{\boldsymbol{v}} + \boldsymbol{v}')) + (\nabla^s\bar{\boldsymbol{w}}, 2\nu\nabla^s(\bar{\boldsymbol{v}} + \boldsymbol{v}')) - (\nabla \cdot \bar{\boldsymbol{w}}, p) - (\bar{\boldsymbol{w}}, \boldsymbol{f}) = 0, \tag{11}$$

$$(q, \nabla \cdot (\bar{\boldsymbol{v}} + \boldsymbol{v}')) = 0, \tag{12}$$

Fine-scale sub-problem:

$$\left(\boldsymbol{w}', \frac{\partial(\bar{\boldsymbol{v}} + \boldsymbol{v}')}{\partial t}\right) - (\nabla\boldsymbol{w}', (\bar{\boldsymbol{v}} + \boldsymbol{v}') \otimes (\bar{\boldsymbol{v}} + \boldsymbol{v}')) + (\nabla^s\boldsymbol{w}', 2\nu\nabla^s(\bar{\boldsymbol{v}} + \boldsymbol{v}')) - (\nabla \cdot \boldsymbol{w}', p) - (\boldsymbol{w}', \boldsymbol{f}) = 0, \tag{13}$$

The key idea underlying the VMS based turbulence models is to solve the fine scale problem (13) locally, and express the fine-scale solution $\boldsymbol{v}'$ in terms of the residual of the Euler–Lagrange equations of the coarse scales $\bar{\boldsymbol{v}}$. Since $\boldsymbol{v}'$ in (13) lies in an infinite dimensional space and that the equation is nonlinear, a closed form expression for $\boldsymbol{v}'$ is not possible. Consequently, in the discrete case, some approximations need to be made to the space of fine scales $\mathcal{V}'$ so as to model $\boldsymbol{v}'$. The modeled fine-scale solution can then be variationally projected onto the coarse-scales space, thereby resulting in a modified formulation for (11), (12) that only depends on the coarse-scale fields. Furthermore, the contributions of the modeled fine-scales get manifested via the additional residual-based terms that play the role of not only stabilizing the formulation, but also modeling the effects of the sub-grid eddies.

A common procedure adopted for the solution of fine-scale velocity field in the VMS-based turbulence models is the use of Green's functions based approaches. For general guidelines on the design of Greens's functions based solutions see Hughes et al. [23], and for an application of the method see Bazilevs et al. [3].

In our work, we treat the fine-scale problem in a rather direct fashion. To find an expression for the fine-scale velocity field we perform linearization of the nonlinear fine-scale problem, and this precludes the need for any a priori assumption on the form of the fine-scale velocity field. Furthermore, our approach to the fine-scale modeling derives from the notion of the residual free bubbles (RFB) method [6,12] which is applied only to the fine-scale problem. A form equivalence between the residual-free bubble methods and the Green's function based methods is presented in Brezzi et al. [5].

3.1. Modeling of the fine scale field

We consider the fine scale problem (13) and apply integration by parts to the skew term:

$$\left(\boldsymbol{w}', \frac{\partial(\bar{\boldsymbol{v}} + \boldsymbol{v}')}{\partial t}\right) + (\boldsymbol{w}', (\bar{\boldsymbol{v}} + \boldsymbol{v}') \cdot \nabla(\bar{\boldsymbol{v}} + \boldsymbol{v}')) + (\nabla^s\boldsymbol{w}', 2\nu\nabla^s(\bar{\boldsymbol{v}} + \boldsymbol{v}')) - (\nabla \cdot \boldsymbol{w}', p) - (\boldsymbol{w}', \boldsymbol{f}) = 0, \tag{14}$$

where we have employed the assumption on $\boldsymbol{w}'$ given in (10) and have directly enforced the continuity Eq. (6). Rearranging (14) we can write:

$$\left(\boldsymbol{w}', \frac{\partial\boldsymbol{v}'}{\partial t}\right) + (\boldsymbol{w}', \boldsymbol{v}' \cdot \nabla\bar{\boldsymbol{v}}) + (\boldsymbol{w}', \bar{\boldsymbol{v}} \cdot \nabla\boldsymbol{v}') + (\boldsymbol{w}', \boldsymbol{v}' \cdot \nabla\boldsymbol{v}') + (\nabla^s\boldsymbol{w}', 2\nu\nabla^s\boldsymbol{v}') = -(\boldsymbol{w}', \boldsymbol{r}), \tag{15}$$

where

$$\boldsymbol{r} = \frac{\partial\bar{\boldsymbol{v}}}{\partial t} + \bar{\boldsymbol{v}} \cdot \nabla\bar{\boldsymbol{v}} - 2\nu\Delta^s\bar{\boldsymbol{v}} + \nabla p - \boldsymbol{f}, \tag{16}$$

is the residual of the Euler–Lagrange equations for the coarse scales. Consequently, the projection of the coarse-scale residual onto the fine scales drives the fine-scale problem. Due to the assumption on the space of functions for the fine scales, this residual is defined over the sum of element interiors.

Eq. (15) presents a time-dependent system of nonlinear equations. To linearize, we use scaling arguments and neglect the higher order term $(\boldsymbol{w}', \boldsymbol{v}' \cdot \nabla\boldsymbol{v}')$. From a computational perspective this amounts to solving the fine scale problem (15) using a single iteration in the Newton–Raphson method for the coarse-scale solution [7]. Assuming the fine-scale velocity to be linear during each of the Newton iterations for the coarse-scales leads to a fine-scale velocity field that scales proportional to the residual, but with a direction that is a linear combination of the directions of the coarse-scale velocity and that of the residual.

We then discretize (15) in time using the generalized alpha method [27]. Consequently, at a given time level n, we can write the discrete system as:

$$\left(\boldsymbol{w}', \left.\frac{\partial\boldsymbol{v}'}{\partial t}\right|_{n+\alpha_m}\right) + \left(\boldsymbol{w}', \boldsymbol{v}'_{n+\alpha_f} \cdot \nabla\bar{\boldsymbol{v}}_{n+\alpha_f}\right) + \left(\boldsymbol{w}', \bar{\boldsymbol{v}}_{n+\alpha_f} \cdot \nabla\boldsymbol{v}'_{n+\alpha_f}\right) + \left(\boldsymbol{w}', \boldsymbol{v}'_{n+\alpha_f} \cdot \nabla\boldsymbol{v}'_{n+\alpha_f}\right) + \left(\nabla^s\boldsymbol{w}', 2\nu\nabla^s\boldsymbol{v}'_{n+\alpha_f}\right) = -(\boldsymbol{w}', \boldsymbol{r}_{n+\alpha_f}), \tag{17}$$

where

$$\left.\frac{\partial \boldsymbol{v}'}{\partial t}\right|_{n+\alpha_m} = \left(1-\frac{\alpha_m}{\gamma}\right)\left.\frac{\partial \boldsymbol{v}'}{\partial t}\right|_{n} + \frac{\alpha_m}{\gamma\Delta t}\left(\boldsymbol{v}'_{n+1}-\boldsymbol{v}'_{n}\right), \tag{18}$$

$$\boldsymbol{v}'_{n+\alpha_f} = (1-\alpha_f)\,\boldsymbol{v}'_{n} + \alpha_f\,\boldsymbol{v}'_{n+1}. \tag{19}$$

In Eqs. (18) and (19), α_m,α_f and γ are the parameters of the generalized alpha method and Δt denotes the time step increment. Substituting (18) and (19) in (17), and moving the terms at time level n to the right hand side of the expression, we get:

$$\begin{aligned}
&\frac{\alpha_m}{\gamma\Delta t}\left(\boldsymbol{w}', \boldsymbol{v}'_{n+1}\right) + \alpha_f\Big\{\left(\boldsymbol{w}', \boldsymbol{v}'_{n+1}\cdot\nabla\bar{\boldsymbol{v}}_{n+\alpha_f}\right) + \left(\boldsymbol{w}', \bar{\boldsymbol{v}}_{n+\alpha_f}\cdot\nabla\boldsymbol{v}'_{n+1}\right)\\
&\quad + \left(\nabla^s\boldsymbol{w}', 2\nu\nabla^s\boldsymbol{v}'_{n+1}\right)\Big\}\\
&= -(1-\alpha_f)\Big\{\left(\boldsymbol{w}', \boldsymbol{v}'_{n}\cdot\nabla\bar{\boldsymbol{v}}_{n+\alpha_f}\right) + \left(\boldsymbol{w}', \bar{\boldsymbol{v}}_{n+\alpha_f}\cdot\nabla\boldsymbol{v}'_{n}\right) + \left(\nabla^s\boldsymbol{w}', 2\nu\nabla^s\boldsymbol{v}'_{n}\right)\Big\}\\
&\quad - \left(1-\frac{\alpha_m}{\gamma}\right)\left(\boldsymbol{w}', \left.\frac{\partial\boldsymbol{v}'}{\partial t}\right|_{n}\right) + \frac{\alpha_m}{\gamma\Delta t}\left(\boldsymbol{w}', \boldsymbol{v}'_{n}\right) - \left(\boldsymbol{w}', \boldsymbol{r}_{n+\alpha_f}\right).
\end{aligned} \tag{20}$$

Remark 5. We have employed the generalized alpha method in the present work. However, other time integration schemes can also be employed in the modeling of the fine scales by following the general procedure presented here.

3.1.1. Evaluating fine-scales via bubble functions approach

In order to solve the discrete problem at time level $n+1$, we assume that the fine scales can be expressed in terms of bubble functions, $b^e(\xi)$, defined over the interior of the elements:

$$\boldsymbol{v}' = \boldsymbol{\beta} b^e(\xi), \tag{21}$$

$$\boldsymbol{w}' = \boldsymbol{\gamma} b^e(\xi), \tag{22}$$

where $\boldsymbol{\beta}$ and $\boldsymbol{\gamma}$ are the coefficients for the fine scale velocity trial solutions and weighting functions, respectively. Because of the definition of the bubble functions, the approximation to the localized fine-scale problem is only valid locally, and therefore assumed to be restricted to the element interiors. Consequently, all inner products containing the fine-scale approximations are restricted to element interiors.

Substituting (21) and (22) in (20), we can solve for the fine scale coefficients $\boldsymbol{\beta}_{n+1}$ and construct the fine scale velocity field as:

$$\begin{aligned}
\boldsymbol{v}'_{n+1}(\boldsymbol{x}) &= b^e\boldsymbol{\beta}_{n+1}\\
&= \left\{\frac{\alpha_m}{\gamma\Delta t}\left(b^e, b^e\right) + \alpha_f\hat{\boldsymbol{\tau}}\right\}^{-1}\begin{bmatrix}\left\{\frac{\alpha_m}{\gamma\Delta t}\left(b^e, b^e\right) - (1-\alpha_f)\hat{\boldsymbol{\tau}}\right\}\boldsymbol{v}'_{n}\\ -\left(1-\frac{\alpha_m}{\gamma}\right)\left(b^e, b^e\right)\frac{\partial\boldsymbol{v}'_{n}}{\partial t}\\ -b^e\left(b^e, \boldsymbol{r}_{n+\alpha_f}\right)\end{bmatrix},
\end{aligned} \tag{23}$$

where $\hat{\boldsymbol{\tau}}$ is defined as:

$$\hat{\boldsymbol{\tau}} = \left[\int (b^e)^2\nabla^T\bar{\boldsymbol{v}}\,\mathrm{d}\Omega + \int b^e\bar{\boldsymbol{v}}\cdot\nabla b^e\,\mathrm{d}\Omega I + \nu\int\left|\nabla b^e\right|^2\mathrm{d}\Omega I + \nu\int\nabla b^e\otimes\nabla b^e\,\mathrm{d}\Omega\right]^{-1}. \tag{24}$$

Remark 6. The tensorial function $\hat{\boldsymbol{\tau}}$ defined in (24) is form identical to the tensorial form of the stabilization function derived in Masud and Calderer [39]. Due to the time dependency of the fine-scale velocity in (7), the spatial stabilization tensor $\hat{\boldsymbol{\tau}}$ is now fully integrated with the temporal terms that emanate from the ODE integrator.

We can write the fine-scale velocity field in an abstract functional form:

$$\boldsymbol{v}'_{n+1}(\boldsymbol{x}) = \mathcal{F}\left(b^e, \hat{\boldsymbol{\tau}}, \boldsymbol{v}'_{n}, \frac{\partial\boldsymbol{v}'_{n}}{\partial t}, \boldsymbol{r}_{n+\alpha_f}\right). \tag{25}$$

The expression for the fine-scale velocity field $\boldsymbol{v}'_{n+1}(\boldsymbol{x})$ is a function of the time history of the fine scales. Furthermore, in the consistently derived fine-scale field given in Eq. (23), the residual $\boldsymbol{r}$ appears inside an integral term. Consequently, a simple definition of the variational operator $\boldsymbol{\tau}$ does not emerge that can be easily compared with the traditional so-called stabilization parameters being used in the literature. In the following we will consider various approximation options for the representation of the fine-scale velocity field that are facilitated by the fully coupled space–time system (25). Specifically, we will investigate the effects of considering the fine scales to be quasi-static, i.e., we will study the effects of ignoring the time-history of the fine scales. When the time history dependence is ignored, Eq. (23) becomes:

$$\boldsymbol{v}'_{n+1}(\boldsymbol{x}) = b^e\boldsymbol{\beta}_{n+1} = -b^e\left\{\frac{\alpha_m}{\gamma\Delta t}\left(b^e, b^e\right) + \alpha_f\hat{\boldsymbol{\tau}}\right\}^{-1}\left(b^e, \boldsymbol{r}_{n+\alpha_f}\right). \tag{26}$$

This reduction in the temporal domain still yields two options in the spatial dimension:

(i) An ability to account for the full spatial variation of the residual, and
(ii) An option to consider a piecewise constant projection of the residual.

If an element-wise constant projection of the residual $\boldsymbol{r}_{n+\alpha_f}$ is considered, the fine-scale velocity field can be expressed as:

$$\boldsymbol{v}'_{n+1}(\boldsymbol{x}) = -b^e\left(b^e, 1\right)\left\{\frac{\alpha_m}{\gamma\Delta t}\left(b^e, b^e\right) + \alpha_f\hat{\boldsymbol{\tau}}\right\}^{-1}\boldsymbol{r}_{n+\alpha_f} = -\boldsymbol{\tau}\boldsymbol{r}_{n+\alpha_f}, \tag{27}$$

where

$$\boldsymbol{\tau} = b^e\left(b^e, 1\right)\left\{\frac{\alpha_m}{\gamma\Delta t}\left(b^e, b^e\right) + \alpha_f\hat{\boldsymbol{\tau}}\right\}^{-1}. \tag{28}$$

It is important to note that (27) yields a simple definition of the variational operator $\boldsymbol{\tau}$. In Section 3.3 we will analyze the structure of this fine-scale operator, while in Section 4.2.1 we will compare its behavior with the stabilization parameter employed in [3].

Moreover, for the case when the fine scales are considered to be fully transient, there is still the option to assume the element-wise constant projection of the residual. In this case, (23) can be simplified to the following form:

$$\begin{aligned}
\boldsymbol{v}'_{n+1}(\boldsymbol{x}) &= b^e\boldsymbol{\beta}_{n+1}\\
&= \left\{\frac{\alpha_m}{\gamma\Delta t}\left(b^e, b^e\right) + \alpha_f\hat{\boldsymbol{\tau}}\right\}^{-1}\begin{bmatrix}\left\{\frac{\alpha_m}{\gamma\Delta t}\left(b^e, b^e\right) - (1-\alpha_f)\hat{\boldsymbol{\tau}}\right\}\boldsymbol{v}'_{n}\\ -\left(1-\frac{\alpha_m}{\gamma}\right)\left(b^e, b^e\right)\frac{\partial\boldsymbol{v}'_{n}}{\partial t}\\ -b^e\left(b^e, 1\right)\boldsymbol{r}_{n+\alpha_f}\end{bmatrix}.
\end{aligned} \tag{29}$$

Remark 7. In the context of incompressible laminar flows [39,7], to simplify the computation of the fine-scale velocity, we found the mean value projection of the element-wise residual to be a good approximation, i.e., $\left(b^e, \boldsymbol{r}_{n+\alpha_f}\right) \simeq \left(b^e, 1\right)\boldsymbol{r}_{n+\alpha_f}$. In turbulence modeling, where fine-scales represent the rapidly fluctuating part of the velocity field, it seems reasonable to consider the full residual. In Section 4, we will numerically study the influence of the mean value of the residual versus the full residual on the computed coarse-scale solution.

Remark 8. Fine-scale velocity in Eq. (27) does not depend on its time history. However it retains a term that explicitly depends on Δt. In Section 4.2, we will study the effects of ignoring the history dependence of the fine scales on the computed coarse-scale solution.

3.2. Variational projection of fine-scales onto the coarse-scale space

Now we consider the coarse-scale problem (11,12). Combining the two equations, rearranging terms and integrating by parts the terms that contain spatial derivatives of the fine-scale velocity field $\boldsymbol{v}'$, the coarse scale problem can be expressed as:

$$B_{Gal}(\bar{\boldsymbol{w}};\bar{\boldsymbol{v}}) + B^{Turb}_{VMS}(\bar{\boldsymbol{w}};\bar{\boldsymbol{v}},\boldsymbol{v}') = F_{Gal}(\bar{\boldsymbol{w}}), \tag{30}$$

where

$$B_{Gal}(\bar{\boldsymbol{w}};\bar{\boldsymbol{v}}) = \left(\bar{\boldsymbol{w}},\frac{\partial\bar{\boldsymbol{v}}}{\partial t}\right) - (\nabla\bar{\boldsymbol{w}},\bar{\boldsymbol{v}}\otimes\bar{\boldsymbol{v}}) + (\nabla^s\bar{\boldsymbol{w}},2\nu\nabla^s\bar{\boldsymbol{v}}) - (\nabla\cdot\bar{\boldsymbol{w}},p) + (q,\nabla\cdot\bar{\boldsymbol{v}}), \tag{31}$$

$$F_{Gal}(\bar{\boldsymbol{w}}) = (\bar{\boldsymbol{w}},\boldsymbol{f}), \tag{32}$$

are the standard Galerkin terms, and

$$B^{Turb}_{VMS}(\bar{\boldsymbol{w}};\bar{\boldsymbol{v}},\boldsymbol{v}') = \left(\bar{\boldsymbol{w}},\frac{\partial\boldsymbol{v}'}{\partial t}\right) - \left(\bar{\boldsymbol{v}}\cdot\nabla\bar{\boldsymbol{w}} + \bar{\boldsymbol{v}}\cdot\nabla^T\bar{\boldsymbol{w}} + \nabla q + 2\nu\Delta^s\bar{\boldsymbol{w}},\boldsymbol{v}'\right) - (\nabla\bar{\boldsymbol{w}},\boldsymbol{v}'\otimes\boldsymbol{v}'), \tag{33}$$

are the contributions of the fine scales to the coarse-scale problem, that plays the dual role of stabilizing the formulation and modeling the effects of the sub-grid scales.

In stabilized methods [21] as well as in the residual-based turbulence methods a *div*-stabilization term is added to the formulation for a more accurate enforcement of the continuity equation or the conservation of mass condition at the element level. This additional term can also be interpreted as the contribution of a fine scale pressure field p' in the framework of a mixed fine-scale problem. Accordingly, we insert the *div*-stabilization term:

$$b_{div}(\bar{\boldsymbol{w}},\bar{\boldsymbol{v}}) = (\nabla\cdot\bar{\boldsymbol{w}},\tau_c\nabla\cdot\bar{\boldsymbol{v}}), \tag{34}$$

to the left hand side of (30). The parameter τ_c is defined in [3] as:

$$\tau_c = (\tau_M\boldsymbol{g}\cdot\boldsymbol{g})^{-1}, \tag{35}$$

where $\boldsymbol{g}$ is a second order tensor that is a function of the isoparametric mapping between the spatial and the referential domains. For our model, we define τ_M to be used in (35), as follows:

$$\tau_M = \frac{1}{3}trace(\boldsymbol{\tau}), \tag{36}$$

where $\boldsymbol{\tau}$ is the stabilization tensor defined in (28) but without the term that contains Δt. The purpose of using a definition of τ_M that is independent of Δt is to obtain a parameter τ_c that is well behaved irrespective of the time-step size.

Accordingly, the modified formulation with the *div*-stabilization term is:

$$B_{Gal}(\bar{\boldsymbol{w}};\bar{\boldsymbol{v}}) + B^{Turb}_{VMS}(\bar{\boldsymbol{w}};\bar{\boldsymbol{v}},\boldsymbol{v}') + \mathrm{b}_{div}(\bar{\boldsymbol{w}},\bar{\boldsymbol{v}}) = F_{Gal}(\bar{\boldsymbol{w}}). \tag{37}$$

Remark 9. The higher order term $(\nabla\bar{\boldsymbol{w}},\boldsymbol{v}'\otimes\boldsymbol{v}')$ was neglected in our earlier work on laminar flows [39,7]. However this term plays a crucial role in the development of residual-based turbulence models presented here.

Remark 10. Motivated by the assumption that the sub-scales are orthogonal to the coarse scales, some residual-based turbulence models [3,13] drop the term $(2\nu\Delta^s\bar{\boldsymbol{w}},\boldsymbol{v}')$. In Section 4.2.3 we will investigate the effects of neglecting this term in the formulation on the computed coarse-scale solution.

Remark 11. The *div*-stabilization term (34) when added to (30) leads to (37). In Section 4.2.2 the effects of including this additional term to the formulation will be studied.

3.3. Structure of the fine-scale variational operator

The structure of the fine-scale variational operator that scales the residual of the Euler–Lagrange equations of the coarse scales is given by Eq. (23). In order to understand the structure of this variational operator and to compare it with the classical "stabilization parameters", it is convenient to consider its reduced form that is attained by employing an element-wise constant projection of the residual $\boldsymbol{r}_{n+\alpha_f}$. This step amounts to using the mean value of the residual over element interiors. In addition if we drop the time history terms, it leads to the fine-scale velocity field that is given by Eq. (27). The definition of the stabilization tensor $\boldsymbol{\tau}$ can now be analyzed in this context:

(1) Tensor $\boldsymbol{\tau}$ has a part which is termed as $\hat{\boldsymbol{\tau}}$ and is defined in Eq. (24). It is composed of the spatial operators of the Navier–Stokes equations acting directly on the fine-scale field. This is because the standard variational multiscale method belongs to the class of homogeneous multiscale methods wherein the same equation governs the coarse and the fine scale fields.
(2) Secondly, and most importantly, Eq. (24) automatically possesses the right order in the advection and the diffusion dominated regimes, i.e., it is $O(1/h)$ and $O(1/h^2)$ in advection and diffusion dominated regions in the solution space, respectively. Attaining the right order in the two flow regimes has been a major design consideration in the development of various stabilization parameters proposed to date [19].
(3) Another important aspect of the derivation is the dependence of $\boldsymbol{\tau}$ on the temporal domain that is naturally facilitated by the continuous-in-time evolution of the fine-scale velocity field.
(4) The spatial and temporal terms in the definition of the stabilization tensor are fully coupled with the coefficients of the ODE integrator. This is due to the direct treatment of fine scales via linearization of the fine-scale field and the subsequent full expansion of the time terms in the coupled space–time fine-scale problem.

Lastly, $\boldsymbol{\tau}$ is interpolated via the bubble function and therefore it becomes zero at the element boundaries. In Section 4.2.1 we will numerically evaluate this $\boldsymbol{\tau}$ and compare it with the state-of-the-art definition of $\boldsymbol{\tau}$ [3] that is commonly used in the VMS community.

Remark 12. An analysis of the spatial component of the stabilization tensor given in Eq. (24) is presented in [39].

4. Numerical tests

The validity and accuracy of the proposed formulation is shown by means of three test problems. The first problem is forced-isotropic turbulent flow, where energy is supplied at a constant rate to the lower velocity modes. This test case is used to check if in the inertial sub-range, the proposed method is transferring energy to shorter wavelengths at the theoretically predicted rate. The second test case is a turbulent channel flow. We use this problem to study the effects of various modeling options, discussed in Section 3, on the physics of the wall-bounded flows. Finally, the third problem investigates the flow around a fixed cylinder at $Re = 3{,}900$. This problem is more complex than the former two because it contains two boundary layers that detach from the cylinder in a statistically periodic fashion.

All through our numerical calculations we have employed the formulation given in Eq. (37) as our baseline method. This formu-

lation accounts for the second derivative term $(2\nu\Delta^s\bar{\boldsymbol{w}}, \boldsymbol{v}')$ and the fine scale pressure field, i.e., the *div*-stabilization term. In addition, the baseline formulation employed in the numerical studies uses the fine scale velocity obtained in (27) that omits the time-history of the fine scales, along with the element-wise mean value of the residual $\boldsymbol{r}$. For test cases where the baseline formulation is not used, we clearly state the changes.

In all the test cases, 8-node hexahedral elements are used, and full numerical quadrature is employed for spatial integration [20]. Standard quadratic bubble function is employed to solve the fine-scale problem. It is important to note that if the same bubble function is employed everywhere in the evaluation of the $\hat{\boldsymbol{\tau}}$ presented in (24), then the skew-symmetric term would vanish for the case of a uniform velocity field. In [37] we proposed a method based on the idea of residual-free bubbles to modify the bubble function that is employed in the weighting function slot of the skew-advection term. In the residual-free bubbles method, a residual-driven problem is solved at the element level [6]. In general, it is not possible to find the exact residual-free bubbles unless the exact solution to the problem is known. Therefore, a method was proposed by Brezzi et al. [6] to approximate the residual free bubbles using pyramidal bubbles wherein the location of the center of the pyramid is evaluated via minimizing the L_1-norm of the residual. Motivated by [6] we define the bubble function that appears in the weighting function slot of the advection term in (24) to be the shape function associated with the most upwinding node of the element. For a detailed description of the procedure for choosing the modified bubble function, see [39].

The time discretization scheme employed here is the generalized alpha method, with parameter $\rho_\infty = 0$. For preconditioning, the default additive-schwartz method (ASM) preconditioner provided in PETSc is used that employs injection restriction and the transpose for interpolation. In addition, the stabilized bi-conjugate method is used to solve the linear systems that arise from the linearization of the nonlinear equations.

4.1. Forced isotropic turbulence

We first consider the forced isotropic turbulence problem. The problem characteristics and the driving mechanism are the same as the ones presented in [3]. Constant power is supplied to the lowest velocity modes of the fluid via external forcing function which is defined as:

$$\boldsymbol{f}(\boldsymbol{x}) = \sum_{\boldsymbol{k},\boldsymbol{k}\neq\boldsymbol{0}}^{|k_i|\leqslant k_f} \frac{P_{in}}{2E_{k_f}} \hat{\boldsymbol{u}}_{\boldsymbol{k}} e^{i\boldsymbol{k}\cdot\boldsymbol{x}}, \tag{38}$$

where i is the imaginary unit, $P_{in} = 62.8436$ is the constant power input to the flow:

$$E_{k_f} = \frac{1}{2} \sum_{\boldsymbol{k},\boldsymbol{k}\neq\boldsymbol{0}}^{|k_i|\leqslant k_f} \hat{\boldsymbol{u}}_{\boldsymbol{k}} \cdot \hat{\boldsymbol{u}}_{\boldsymbol{k}}, \tag{39}$$

is the contribution of the lowest velocity modes to the kinetic energy, and

$$\hat{\boldsymbol{u}}_{\boldsymbol{k}} = \frac{1}{|\Omega|} \int_\Omega \boldsymbol{u}(\boldsymbol{x}) e^{-i\boldsymbol{k}\cdot\boldsymbol{x}} d\Omega, \tag{40}$$

are the Fourier coefficients of velocity associated with wavenumber $\boldsymbol{k}$. The parameter k_f, which is the threshold that defines the limit of the lowest modes, is set equal to 2.

The computational domain is a cube of length 2π with periodic boundary conditions applied at the six faces. Kinematic viscosity ν is set equal to 1/150, and therefore, the Taylor miscroscale Reynolds number Re_λ is 165. The domain is discretized with uniform meshes of 32^3 and 64^3 hexahedral elements. Time step Δt is set equal to 5×10^{-3} and 2.5×10^{-3} for the two meshes, respectively.

The problem is allowed to evolve in time until a dynamically equilibrated state is reached. Once in the dynamically equilibrated region, the problem is run for additional time steps, and following the guidelines given in [3], statistical data is collected. We observed that 10 units of time are enough to reach the statistically equilibrated state. The average kinetic energy density q of the problem is obtained as:

$$q^2 = \frac{1}{2|\Omega|} \int_\Omega \boldsymbol{u}(\boldsymbol{x}) \cdot \boldsymbol{u}(\boldsymbol{x}) d\Omega. \tag{41}$$

In all the three meshes, q is about 41.5 ± 20% which agrees with the values reported in [3]. Fig. 1(a) shows velocity streamlines and vorticity isosurfaces at a given time level obtained with 64^3 mesh. Details of the vorticity structures surrounded by velocity streamlines

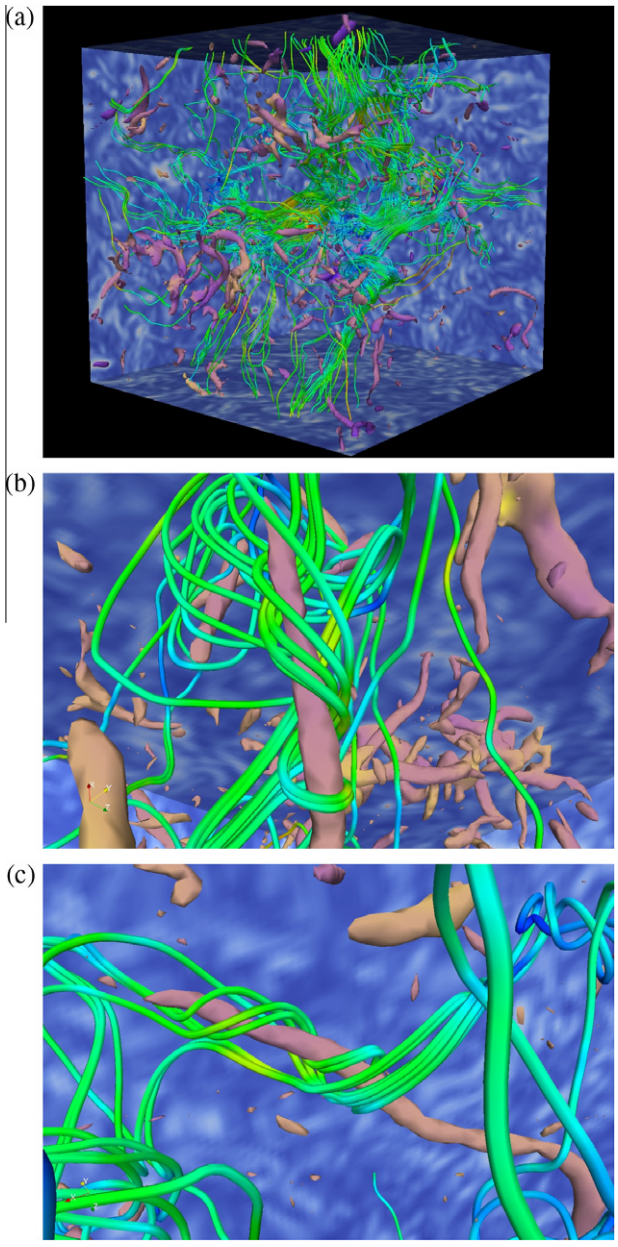

Fig. 1. Vorticity isosurfaces and velocity streamlines, 64^3 elements mesh: (a) full view of the problem domain, (b and c) two different closeup views.

can be observed in Fig. 1(b) and (c). Fig. 2 shows the Fourier transform of the auto-correlation function, which confirms that the rate at which energy is transferred to the higher wavenumbers coincides with the theoretically predicted rate.

The two-point third-order correlation function, which is represented in Fig. 3, is defined as:

$$S_3(r) = \left\langle (u_i(\boldsymbol{x} + r\boldsymbol{e}_i) - u_i(\boldsymbol{x}))^3 \right\rangle, \tag{42}$$

where u_i and $\boldsymbol{e}_i$ are the ith components of the velocity and the unit vector in the ith direction, respectively. As can be seen in Fig. 3, our solution converges to the DNS solution as the mesh is refined.

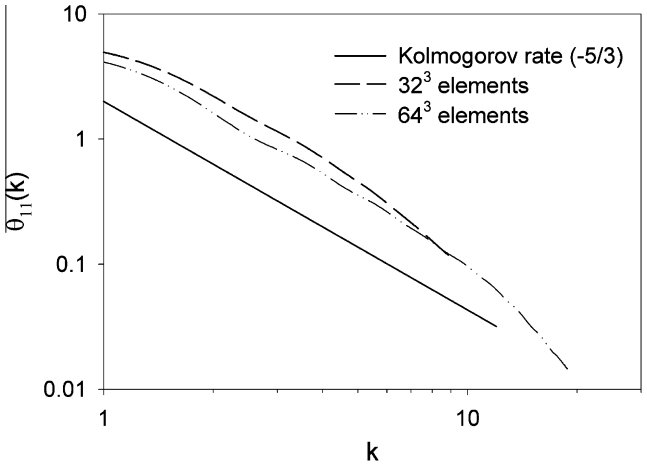

Fig. 2. Fourier transform of the 1D auto-correlation function.

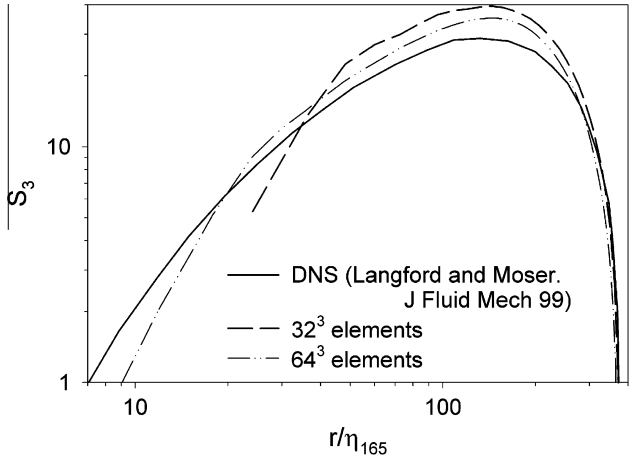

Fig. 3. Two-point third order correlation function.

4.2. Turbulent channel flow

Turbulent channel flow is a standard benchmark problem for evaluating the accuracy of turbulence models in wall bounded flows. In this section channel flow is studied for two different Reynolds numbers, $Re_\tau = 395$ and $Re_\tau = 590$. Results are compared with DNS results of Moser and co-workers [41], with VMS results [3,13] and with LES results obtained with a dynamic Smagorinsky model [13]. Furthermore, in the context of the turbulent channel flow we study the behavior of our fine scales models and investigate the various modeling options that were discussed in Section 3. The modeling options that we use in the following sections are summarized in Table 1.

We consider a hexahedral channel with dimensions $L_x \times L_y \times L_z$. No-slip boundary conditions are prescribed at the walls that are normal to the y-direction. Periodic boundary conditions are prescribed along the other two directions. A constant body force, $\boldsymbol{f}$, is applied to the fluid along the x-direction. Fig. 4 shows a schematic representation of the channel. We consider a flow where $f_x = 0.00337204$ and $\nu = 0.0001472$. Based on the wall units [45], Reynolds number is $Re_\tau = 395$. For the second flow case that we study, we set $f_x = 1.0$ and $\nu = 0.001694915$, which leads to $Re_\tau = 590$. For the $Re_\tau = 395$ flow, the dimensions of the channel are $2\pi \times 2 \times (2/3)\pi$, and for the $Re_\tau = 590$ flow, channel dimensions are $2\pi \times 2 \times \pi$.

The domain is discretized with meshes of 32^3 and 64^3 hexahedral elements. The elements are uniformly distributed in the x and z-directions, while in the wall-normal direction, elements are graded using a hyperbolic stretching. With the exception of Section 4.2.5, where a time step study is carried out, we set time step $\Delta t = 0.025$ for $Re_\tau = 395$ flow, and $\Delta t = 0.0015$ for $Re_\tau = 590$ flow.

The simulations are initialized with a perturbed Poiseuille flow. For each of the cases presented below, the problem is run until a statistically steady state regime is reached. Once the flow is in the statistically steady state regime, the simulation is continued and the solution is sampled every 10 time steps.

4.2.1. Numerical study of the stabilization tensor

In Section 3 the fine-scale field is modeled using a bubble-functions approach, while other residual-based turbulence models compute the fine-scale velocity field using Green's functions along with heuristic simplifications [3]. Here we compare our derived stabilization tensor $\boldsymbol{\tau}$ obtained from (27) with the one used in [3], which is expressed as:

$$\boldsymbol{\tau} = \tau_M \boldsymbol{I}. \tag{43}$$

The parameter τ_M is defined as:

$$\tau_M = \left(\frac{4}{\Delta t^2} + \bar{\boldsymbol{v}} \cdot \boldsymbol{G} \bar{\boldsymbol{v}} + C_I \nu^2 \boldsymbol{G} : \boldsymbol{G} \right)^{-1/2}, \tag{44}$$

Table 1
Summary of numerical models employed in each of the subsections of the turbulent channel flow problem.

Section	Purpose of the section	Observations	Fine-scales
4.2.1	Compare behavior of $\boldsymbol{\tau}$ defined in Eq. (28) with $\boldsymbol{\tau}$ defined in [3]	–	–
4.2.2	Study the effect of p'	Fine-scales are quasi-static, non-orthogonal and mean residual is employed	(27)
4.2.3	Study the effect of the mean-value of the residual vs. the full variation of it	Fine-scales are quasi-static and non-orthogonal. p' is included	(26) and (27)
4.2.4	Study the effect of using orthogonal fine-scales vs. non-orthogonal fine-scales	Fine-scales are quasi-static, and mean residual is employed. p' is included	(27)
4.2.5	Study the effect of considering transient fine-scales vs. quasi-static fine-scales	Fine-scales are non-orthogonal and mean residual is employed. p' is included	(27) and (29)

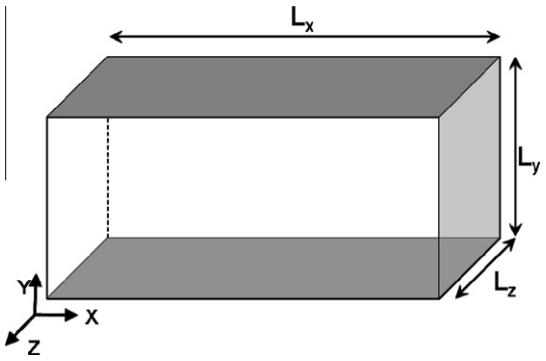

Fig. 4. Schematic representation of the channel.

where the second order tensor $\boldsymbol{G}$ is defined as:

$$G_{ij} = \sum_{k=1}^{3} \frac{\partial \xi_k}{\partial x_i} \frac{\partial \xi_k}{\partial x_j}, \tag{45}$$

in which $\boldsymbol{x} = \boldsymbol{x}(\xi)$ is the mapping between the coordinates $\boldsymbol{\xi} = \{\xi_i\}_{i=1}^{3}$ expressed in the isoparametric space of the element and the coordinates $\boldsymbol{x} = \{x_i\}_{i=1}^{3}$ expressed in the physical space.

For the turbulent channel flow at $Re_T = 395$, Fig. 5(a) shows the stabilization parameter plotted along a line orthogonal to the walls that have been prescribed no-slip boundary condition. This line passes through the centerline of a column of elements. Since the stabilization parameter in (27) is premultiplied by the bubble function, it attains a value $\boldsymbol{\tau} = 0$ along element boundaries. Accordingly, the intercept along horizontal axis in Fig. 5(a) represents the inter-element boundaries. The mesh employed for turbulent channel flow is graded in the wall normal direction, and therefore we see the graded spatial support for the bubbles, i.e., we observe a reduction in $\tau_{\max}(\Omega^e)$ close to the bounding wall. Since our stabilization parameter is in fact a tensor quantity, we use one third of the trace of the tensor for comparison purposes. Also plotted is the classical τ_M [3] defined in (44). For comparison, in Fig. 5(b) we plot the element-wise mean value of the parameter $\tau_{AVG} = \frac{1}{meas\Omega^e} \int_{\Omega^e} \frac{1}{3} trace(\boldsymbol{\tau}) d\Omega$ in the wall normal direction. The figure shows that the value of τ_{AVG} over the element is in the same range as the value of τ_M from (44) and therefore our derived stabilization tensor behaves analogous to the classical stabilization parameter [19,3]. In our numerical implementation, we have employed the full $\boldsymbol{\tau}$ that varies over the element because of composition with the bubble function.

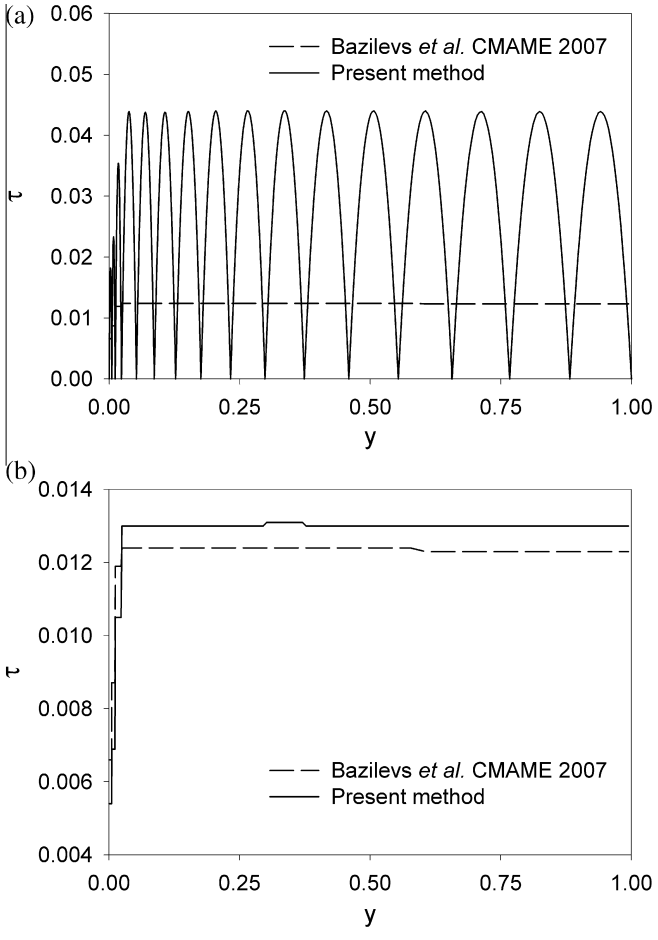

Fig. 5. Comparison of stabilization parameter: (a) actual computed value, (b) averaged value over the element.

4.2.2. Study of the effects of accounting for the fine-scale pressure field

Eq. (30) is the result of considering a multiscale decomposition of the velocity field alone, i.e., a decomposition of the pressure field into coarse and fine-scale pressures is not considered. Some residual-based turbulence models assume the existence of a fine-scale pressure field [3], that manifests itself as an additional term that is proportional to the divergence of the coarse-scale velocity field. Consequently, it results in a more accurate enforcement of conservation of mass in an element wise fashion. In order to have a better enforcement of the continuity equation, we have added a *div*-stabilization term in (30), which yields a modified formulation (37). The purpose of the present section is to study the influence of this additional term, and therefore of the assumption of the existence of a fine-scale pressure field on the computed large-scale features of the VMS-based turbulence model. For the simulations presented in this section, we have employed an element-wise constant projection of the coarse-scale residual given in Eq. (27) that ignores the time-history of the fine scales.

For the turbulent flow at $Re_T = 395$ and for the 32^3 elements mesh, Fig. 6 shows snapshots of the streamlines and vorticity isosurfaces at various time levels. Also presented is the velocity field projected onto the walls of the channel. The convection of massless particles in the boundary layer region is shown and the particles are color coded to indicate their age as the simulation progresses. The boundary layer region is clearly evident and the effect of turbulent fluctuations can be observed via the randomness in the motion of the particles as they age.

Fig. 7 shows the mean-stream velocity and the root mean square (RMS) of the fluctuations of the velocity field for the 32^3 elements mesh. Both of our formulations (30) and (37) are considered. The results are compared with the DNS results of Moser et al. [41]. For comparison purposes, Fig. 7 also includes results obtained with a Smagorinsky model [13] and VMS results reported by Bazilevs and co-workers [3] using a mesh of trilinear hexahedral 32^3 elements, where a fine scale pressure field was included. Fig. 7 also shows the results presented in [3] using an equivalent mesh but with cubic NURBS. We see that our results with p' are similar to the results reported in [3] for linear elements. It can also be observed that the mean-stream velocity and the fluctuations in the stream-wise and wall-normal directions are better captured with the formulation that does not consider the fine-scale pressure field (30). However, as we show in Table 2, not accounting for the fine-scale pressures results in an increase in the error in an element-wise enforcement of the continuity equation. Fluctuations of the velocity in the span-wise direction are represented equally well with both the formulations (30) and (37).

Fig. 8 shows a study carried out using a 64^3 elements mesh and comparison is done with the results obtained with the cruder mesh of 32^3 elements. Fig. 9 shows results for the turbulent channel flow at a higher Reynolds number $Re_T = 590$ for the 64^3 hexahedral

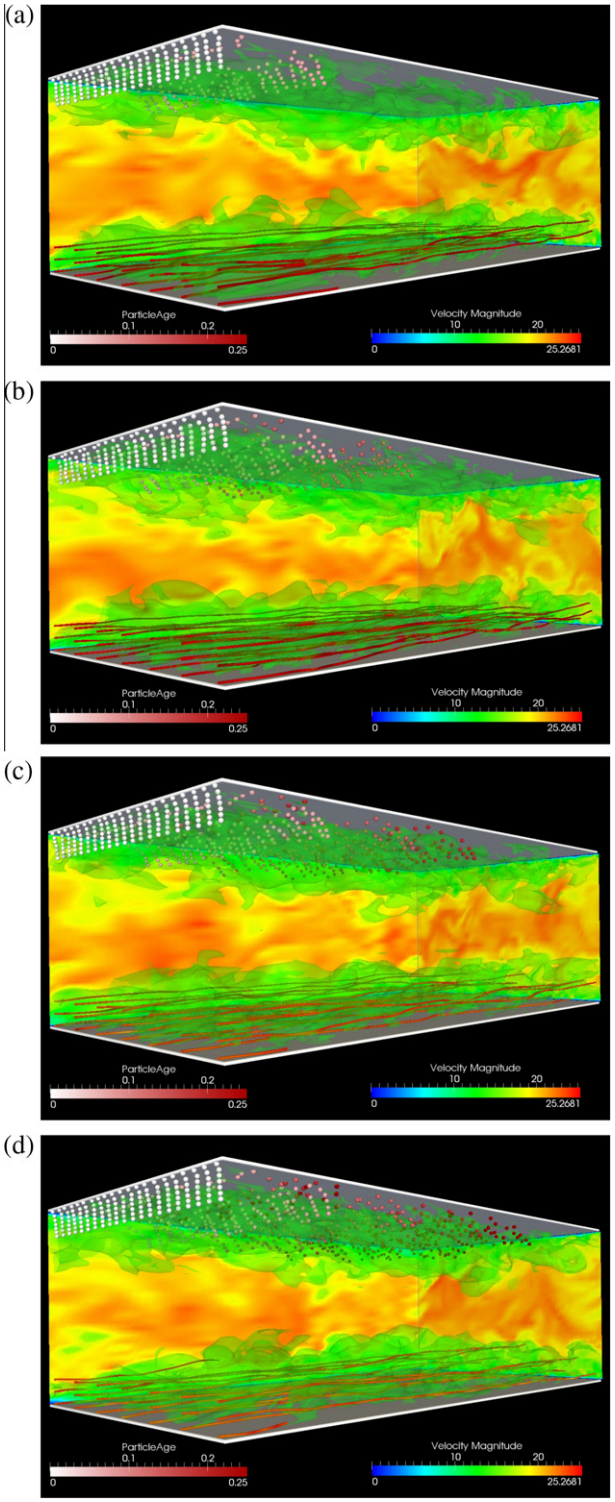

Fig. 6. (a–d) Streamlines, vorticity isosurfaces, velocity field projected onto the walls, and massless particles in the boundary layer region for the turbulent channel flow at $Re_T = 395$ (32^3 elements mesh).

elements mesh. As can be seen, formulation (37) performs better than the results obtained with a VMS model presented in [13] where 64^3 hexahedral elements mesh was also used.

Remark 13. It is well documented in the literature that lower order Lagrange elements have a propensity for volumetric locking when the incompressibility condition given in Eq. (2) is strongly

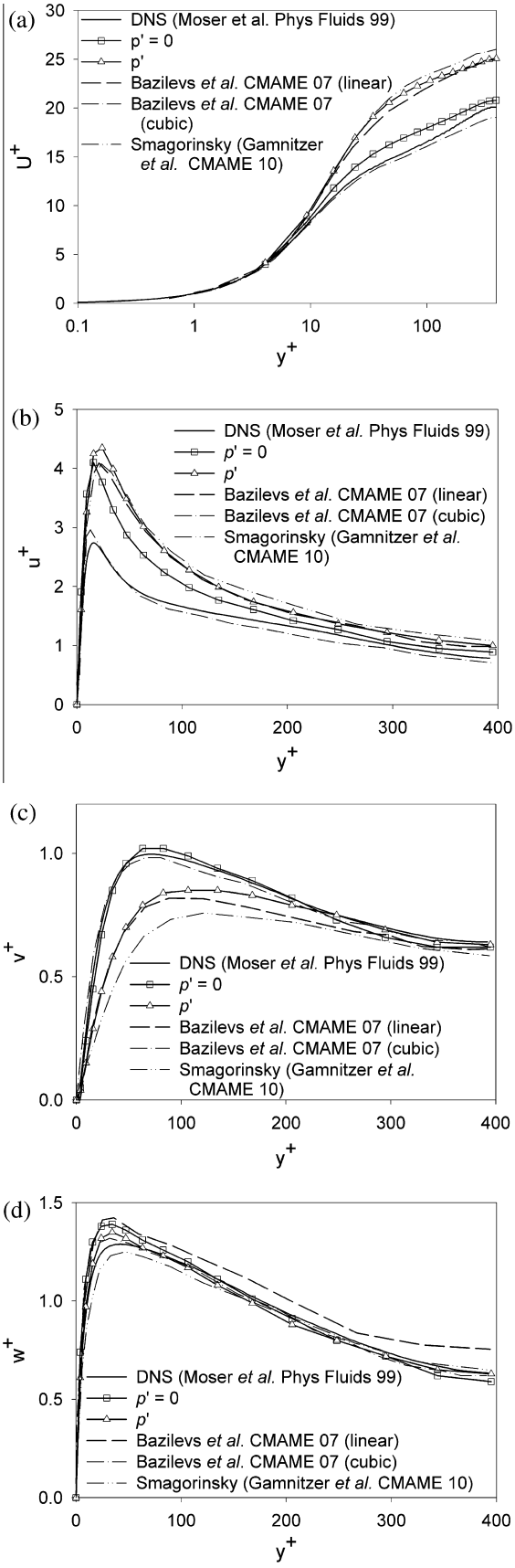

Fig. 7. Effects of accounting for the fine-scale pressure field. $Re_T = 395$ (32^3 elements mesh): (a) mean stream-wise velocity. RMS of the velocity fluctuations in: (b) the stream-wise, (c) the wall-normal and (d) the span-wise directions.

Table 2
Time-averaged L_2-norm of the divergence of the velocity $\langle \|\nabla \cdot \bar{\boldsymbol{v}}\|_{L_2} \rangle_t / \|1\|_{L_2}$.

	$p' = 0$	p'
$Re_T = 395$ (32^3 elements mesh)	1.49×10^{-1}	1.93×10^{-2}
$Re_T = 590$ (64^3 elements mesh)	6.32×10^{2}	1.67×10^{1}

enforced [20, Chapter 4]. On one hand the fine-scale pressures that manifest themselves in the form of an additional *div*-stabilization term help in the enforcement of the continuity equation, on the other hand they tend to make the response rather overly stiff. We see these effects in Fig. 7 where ignoring the *div*-stabilization term results in a flexible response that is better able to represent the mean flow statistics as well as the fluctuations. However, considering the relative importance of satisfying the continuity equation, we consider formulation (37) that accounts for p' as our base formulation hereon.

As discussed in Section 3, adding a fine-scale pressure field is a way to strengthen the continuity constraint. Table 2 shows the time averaged L_2-norm of the divergence of the velocity field, $\langle \|\nabla \cdot \bar{\boldsymbol{v}}\|_{L_2} \rangle_t$. It can be seen that, although the mean velocity field and its fluctuations are invariably better captured with the formulation that does not account for the fine-scale pressure field p', the incompressibility constraint is better satisfied if the fine-scale pressure is taken into account. Satisfaction of the incompressibility constrain is an important consideration in the solution of the incompressible Navier–Stokes equations, as it is directly related to the satisfaction of the local conservation of mass. As presented in Table 2, an increase in Re_T results in a reduction in the accuracy of the local conservation property. Consequently, accounting for this term, especially for higher Re_T flows would seem necessary.

4.2.3. Study of the effect of employing the mean-value of the residual

In Section 3.2, where the fine-scale problem is modeled, the representation of the fine-scale velocity field can be simplified by assuming an element-wise constant projection of the residual of the coarse-scale equations. If the full residual is taken into account, then fine-scale solution is exactly a quadratic bubble function. However, if the mean-value projection is considered, then the fine-scale solution is a modulated quadratic bubble function. In this section we study the effects of the reduced order projection of the element-wise residual on the statistics of the numerical solution for the turbulent channel flow at $Re_T = 395$. Specifically, we use the mean-value based fine-scale field given in (27), and compare it with the case wherein the full residual is employed only in the higher-order terms in (26) while in the rest of the terms we still consider the mean-value based residual. We employ our standard formulation (37) that takes into account the fine-scale pressure term, and also ignore the time-history of the fine-scales in the evaluation of the fine scales. Fig. 10 shows the statistics for the two cases. In both cases, the 32^3 elements mesh is employed. It can be seen that there is no appreciable improvement in the solution even if the full residual is used.

4.2.4. Study of the effects of the orthogonality of sub-scales

To study the effects of the orthogonality of sub-scales with respect to the coarse scale space, we investigate the flow at $Re_T = 395$. We employ our standard formulation (37) that accounts for the term $(2\nu\Delta^s\bar{\boldsymbol{w}}, \boldsymbol{v}')$, and compare it with the case wherein fine-scales are orthogonal to the coarse-scales, thereby, annihilating $(2\nu\Delta^s\bar{\boldsymbol{w}}, \boldsymbol{v}')$. For this study we have employed an element-wise constant projection of the coarse-scale residual given in Eq. (27) wherein history dependence of fine-scales is suppressed. The study was performed using the 32^3 elements mesh. Fig. 11 shows the

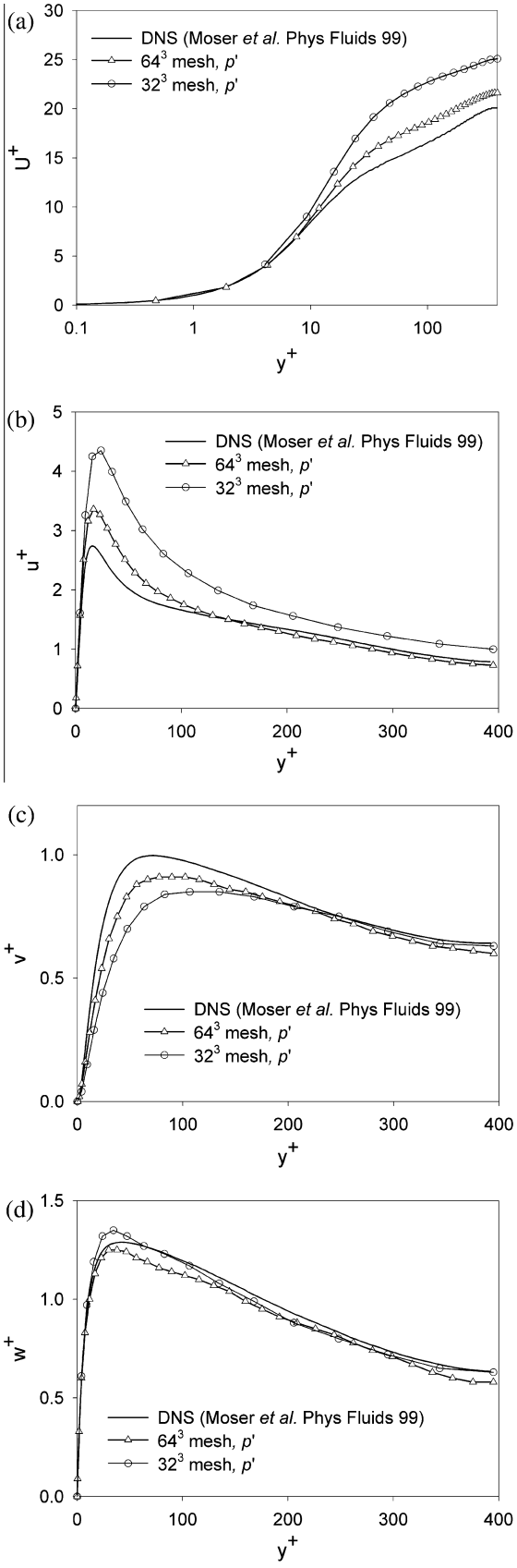

Fig. 8. Effects of mesh refinement on the computed solution. $Re_T = 395$ (32^3 and 64^3 elements meshes): (a) mean stream-wise velocity. RMS of the velocity fluctuations in: (b) the stream-wise, (c) the wall-normal and (d) the span-wise directions.

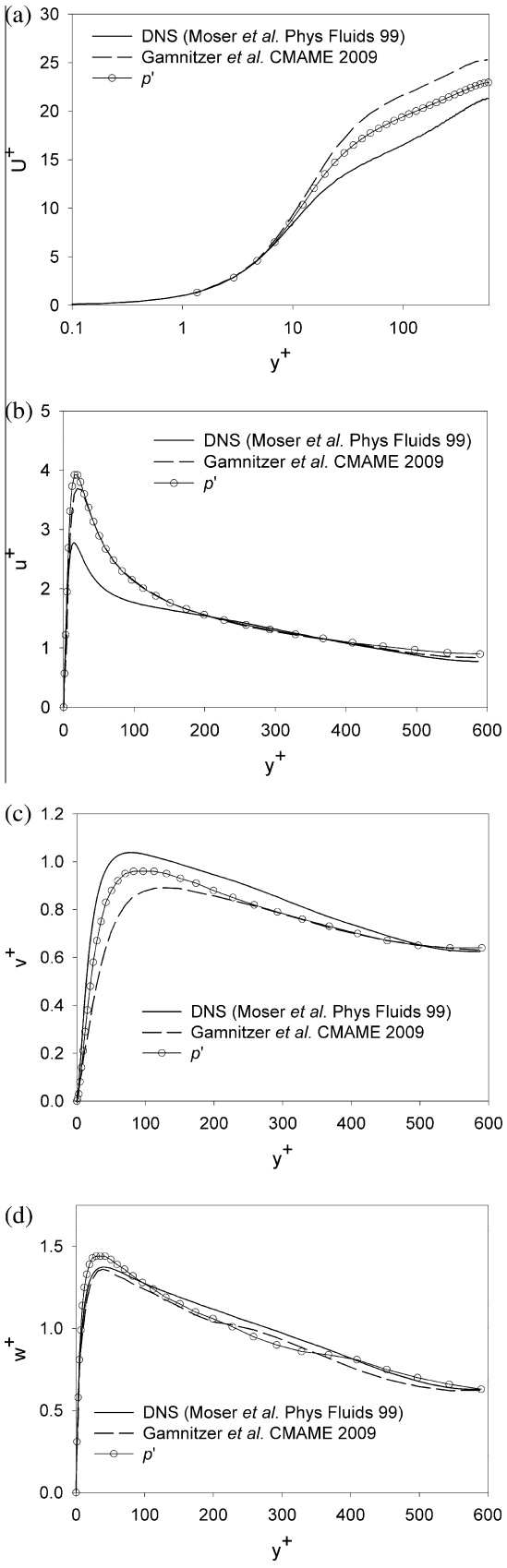

Fig. 9. Effects of accounting for the fine-scale pressure field. $Re_\tau = 590$ (64^3 elements mesh). (a) Mean stream-wise velocity. RMS of the velocity fluctuations in: (b) the stream-wise, (c) the wall-normal and (d) the span-wise directions.

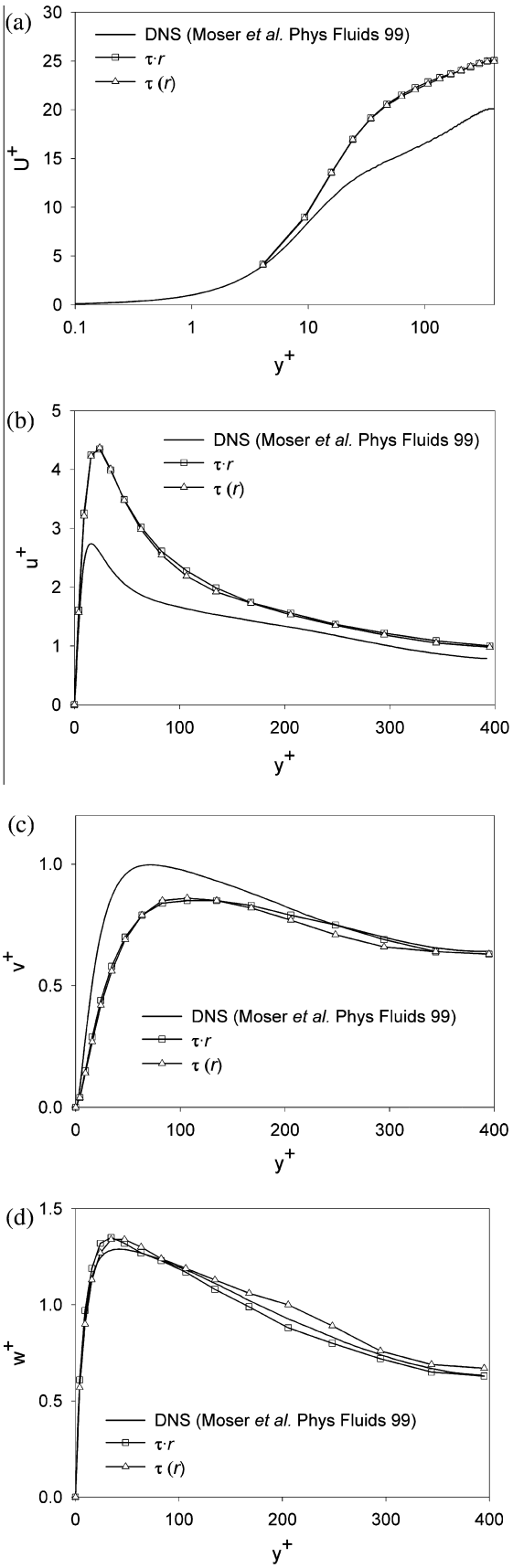

Fig. 10. Effects of considering a constant-projection of the residual: (a) mean stream-wise velocity. RMS of the velocity fluctuations in: (b) the stream-wise, (c) the wall-normal and (d) the span-wise directions.

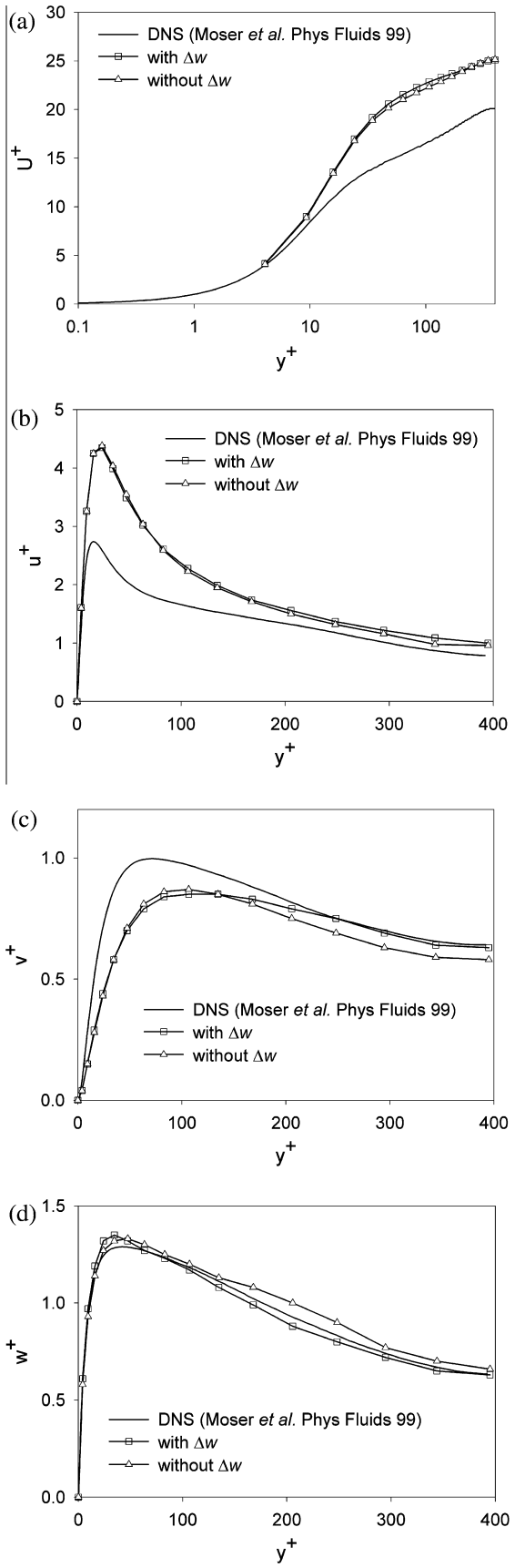

Fig. 11. Effects of considering orthogonal sub-scales: (a) mean stream-wise velocity. RMS of the velocity fluctuations in: (b) the stream-wise, (c) the wall-normal and (d) the span-wise directions.

statistics for the two formulations, where the two results are practically coincident.

Remark 14. With a view that the fine scale viscosity term $(2\nu\Delta^s\bar{\boldsymbol{w}}, \boldsymbol{v}')$ might be introducing excessive fine scale dissipation, the notion of the orthogonality of sub-scales with respect to the coarse scale space has been employed in the literature as a means to annihilate this term.

4.2.5. Study of the effects of neglecting the time-history of fine-scales

As was discussed in Section 3, Eq. (25) offers several options for the time-dependent fine scale velocity field. Specifically, two models for the velocity fine scales are considered. In the reduced model, given in (27), the time history of the fine-scales is neglected, however the variational operator $\boldsymbol{\tau}$ still retains the dependence on Δt. In the full model, given in (23), the fine scales are time-dependent and they need to be tracked at Gauss points if an element-wise constant projection of the residual is to be considered. The version of the full model presented in this section assumes an element-wise constant projection of the residual (29).

To compare the two models we analyze the turbulent channel flow at $Re_T = 395$ and perform a time step study with $\Delta t = 0.025$ and 0.00625. For the case of dynamic fine-scales, a smaller time step of $\Delta t = 0.0015625$ is also employed. In both the cases, the 32^3 elements mesh is employed. Fig. 12 shows the results obtained with the first model that omits the history dependence of the fine scales. It can be seen that as Δt is decreased, the results do not uniformly converge. The degradation in accuracy as Δt is decreased is clearly manifested via the fluctuations in the wall-normal and span-wise velocities in Fig. 12(c) and (d), respectively. This anomaly can be explained by observing Eq. (27), where in the limit $\Delta t \to 0$ the fine scales vanish, and as a consequence, the stabilization terms in the formulation also vanish. On the other hand, Fig. 13 shows that for the model that accounts for the history dependence of fine-scale field, very small time steps do not degrade the accuracy of the solution. Similar behavior for analogous models has also been reported in Hsu et al. [18] and Gamnitzer et al. [13].

It is important to note that the computation of quasi-static fine scales is computational economical as compared to the dynamical fine scales. Therefore, when larger time-step sizes can be accommodated, dropping the time history of the fine scales leads to a computationally economic option. On the other hand, the quasi-static fine scales show a pathological behavior when a very small time step-size is employed. Consequently, for the cases wherein very small time-steps are necessary, the model that takes into account the history of the fine-scales should be used as it yields more accurate results.

4.3. Turbulent flow around a fixed cylinder

Viscous flow around a circular cylinder at sufficiently high Reynolds number is a classical benchmark problem that leads to periodic vortex shedding commonly known as the Karman vortex street. In this section we study the flow around a circular cylinder in the turbulent regime and compare our results with the LES results reported in Kravchenko and Moin [30]. In [30], a numerical method based on B-splines was employed. We also compare our results with experimental data reported in Ong and Wallace [44] and with experiments reported in [30] that were conducted by Norberg, and Lourenco and Shish.

We consider a unit diameter cylinder that is centered in the domain as schematically presented in Fig. 14. Viscosity is set equal to 2.5641×10^{-4}. The Reynolds number based on the inflow velocity and diameter of the cylinder is 3,900. No-slip boundary condition

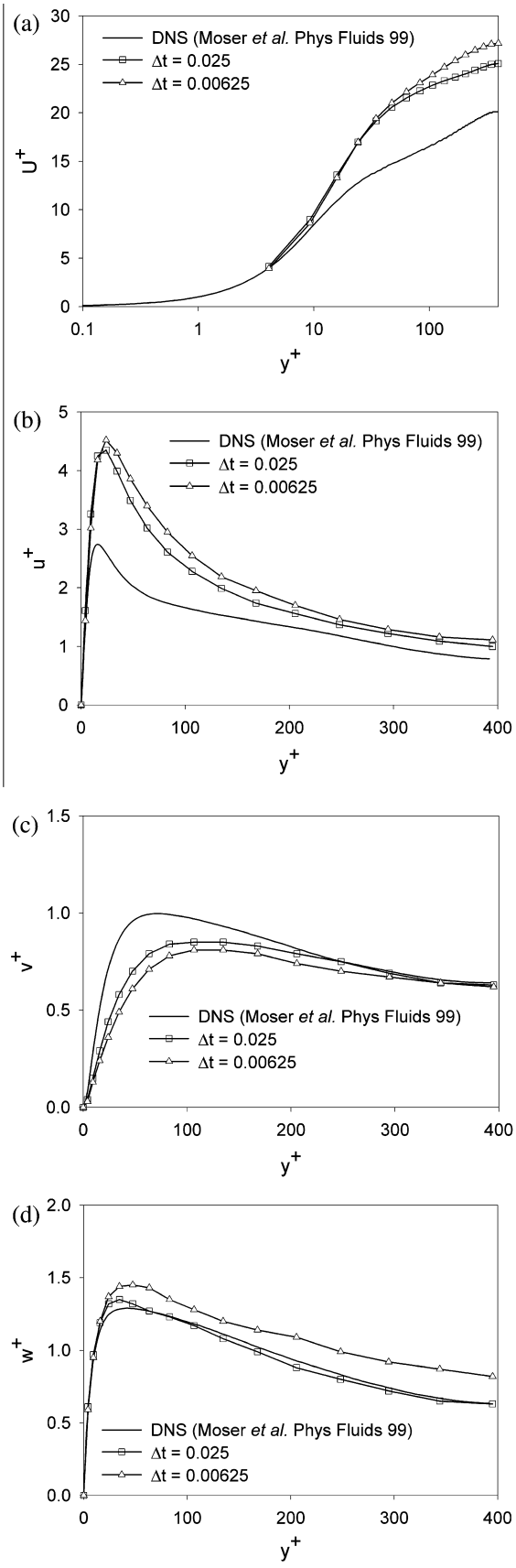

Fig. 12. Study of Δt refinement when dynamic effects of fine-scales are partly neglected: (a) mean Stream-wise velocity. RMS of the velocity fluctuations in: (b) the stream-wise, (c) the wall-normal and (d) the span-wise directions.

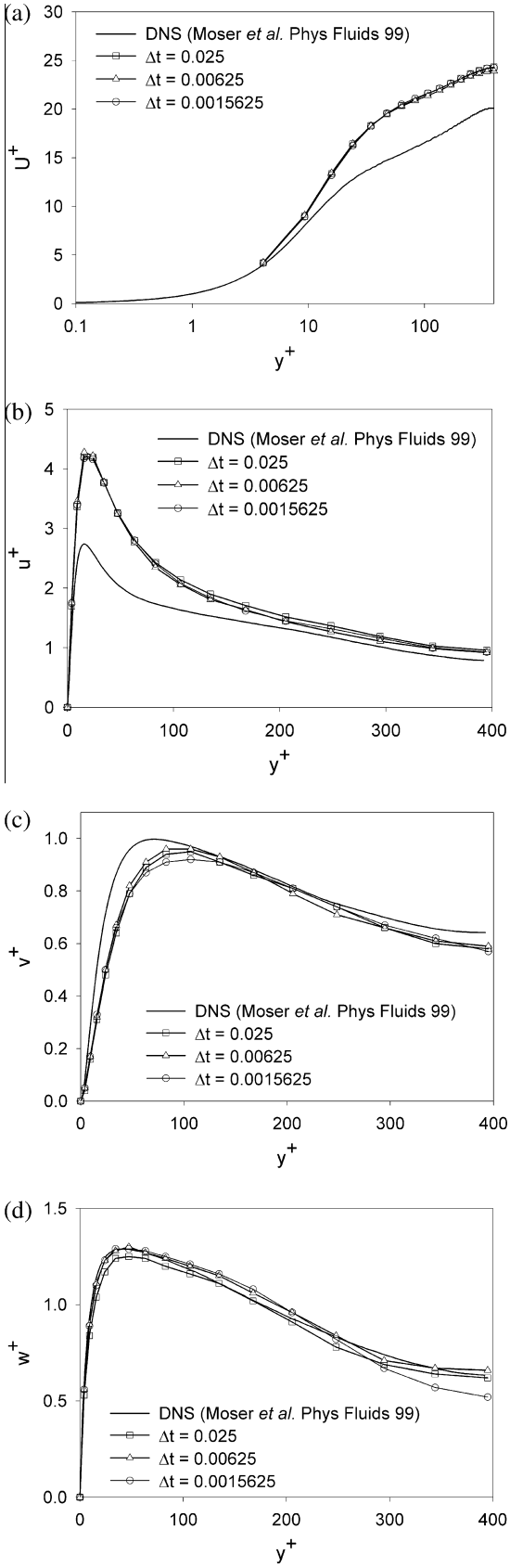

Fig. 13. Study of Δt refinement when all dynamic effects of fine-scales are considered: (a) Mean stream-wise velocity. RMS of the velocity fluctuations in: (b) the stream-wise, (c) the wall-normal and (d) the span-wise directions.

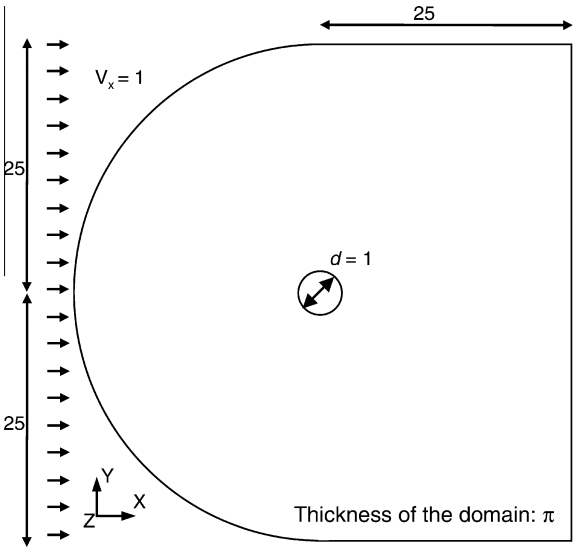

Fig. 14. Schematic representation of the cylinder problem.

is imposed on the surface of the cylinder. Velocity on the inflow boundary is set equal to 1, periodic boundary conditions are imposed in the z-direction, while no-penetration and zero tangential stress conditions are prescribed on the lateral walls. Zero stress is prescribed on the outflow boundary.

Following the guidelines given in [30], the domain is discretized in 48 layers of elements. Each layer approximately contains 160 elements in the radial direction and 250 elements in the circumferential direction. This gives rise to a mesh that consists of 2,436,819 nodes and 2,370,144 hexahedral elements. The mesh is uniform in the direction of the axis of the cylinder and graded in the other directions so that the region with the highest density of elements lies downstream from the cylinder. Details of the mesh around the cylinder can be seen in Fig. 15. Time step Δt is set equal to 0.0025.

The grid employed in [30] has 1,333,472 points. In its local resolution it is comparable to the meshes considered in this section in the vicinity of the cylinder and in its wake. However, the present meshes have more elements in the rest of the domain. A better mesh generator would have yielded an optimal mesh with lesser grid points than are there in our meshes.

In this subsection we have employed the formulation that includes the fine-scale pressure field. However, we have opted to ignore the time history of the fine scale velocity field.

Starting from a zero initial velocity, the problem is allowed to evolve until the main features of the flow are fully developed. Fig. 16 shows that the flow consists of two laminar boundary layers that detach from the cylinder and transition into turbulent layers downstream from it. Fig. 16(a) and (b) show vorticity isosurfaces

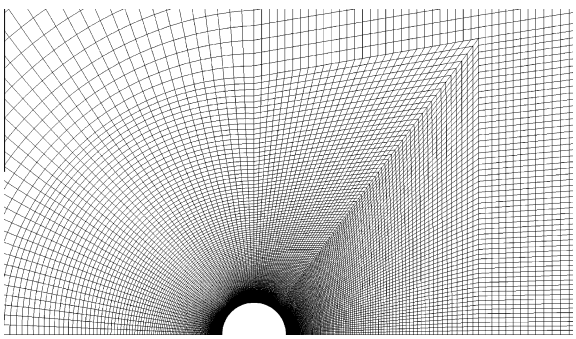

Fig. 15. Plan zoomed view of the upper half of the mesh around the cylinder.

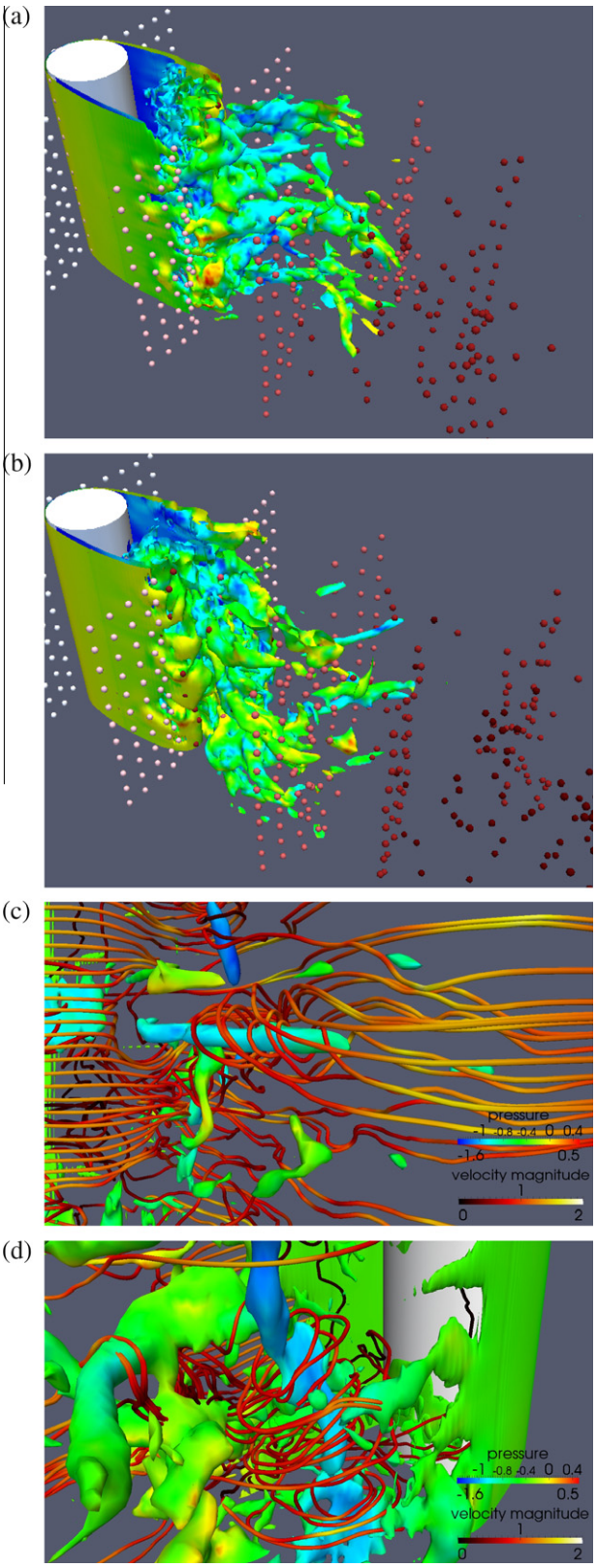

Fig. 16. (a, b) Vorticity isosurfaces colored with the velocity field at two different time instants, and (c, d) zoomed view of velocity streamlines and vorticity isosurfaces where velocity magnitude is employed to color the streamlines and pressure is employed to color the isosurfaces.

at two instants of time that are approximately half cycle apart. During the post processing of the data, massless particles were injected in a plane located upstream of the cylinder. The sequence

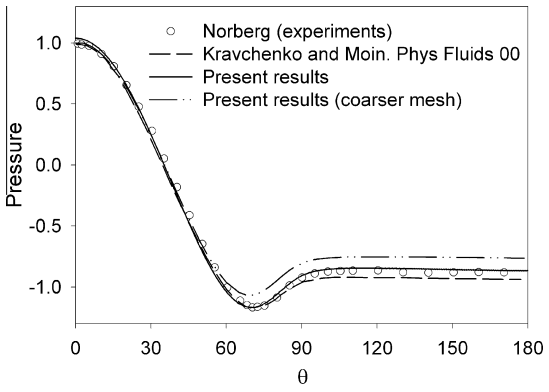

Fig. 17. Mean pressure on the surface of the cylinder. The stagnation point corresponds to $\theta = 0$.

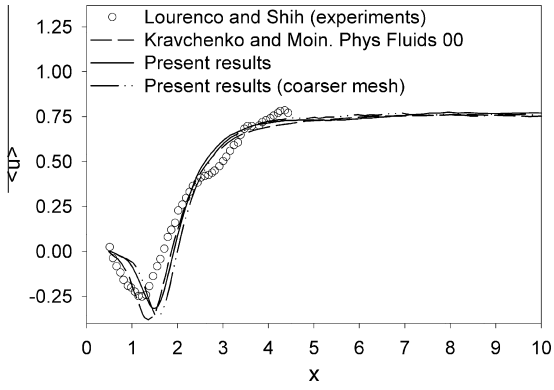

Fig. 18. Mean velocity along the stream-wise direction $y = 0$.

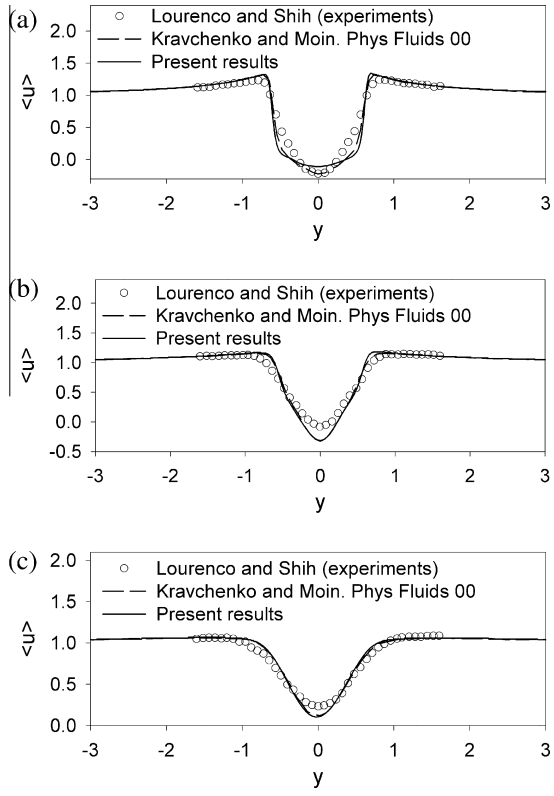

Fig. 19. Mean stream-wise velocity along: (a) $x = 1.06$, (b) $x = 1.54$ and (c) $x = 2.02$.

of images 16(a) and (b) show that, as time progresses, the particles are convected by the fluid and they reveal the turbulent regime of the flow downstream from the cylinder. The color of the particles indicates their age, with the darkest particles being the oldest. Likewise, images 16(c) and (d) show zoomed view of velocity streamlines and vorticity isosurfaces where velocity magnitude is employed to color the streamlines, and pressure is employed to color the isosurfaces.

Once the flow is fully developed, it is sampled every 20 time steps for the next 30 units of time. The statistics of the velocity and pressure fields of the fluid are computed by averaging the solution fields over time and over space along the direction of the axis of the cylinder; a direction in which the flow is homogeneous. Fig. 17 shows the mean pressure field on the surface of the cylinder. The results are comparable with the *B*-spline results and Norberg's results [30]. Fig. 17 also shows the results obtained with the present formulation but with a mesh that consists of 1,854,720 nodes and is much coarser in the boundary layer region compared to our base mesh. A good agreement with [30] can also be observed in Fig. 18, where the mean velocity is plotted along the *x*-direction. Fig. 18 also contains the result obtained with our coarser mesh. Fig. 19 shows the mean stream-wise velocity along three different transverse sections located at $x = 1.06$, $x = 1.54$ and $x = 2.02$ with respect to the center of the cylinder. Analogously, Fig. 20 shows the mean transverse velocity along the same three transverse sections. Fig. 21 plots the mean stream-wise velocity along the sections $x = 6.0$, $x = 7.0$ and $x = 10.0$ with respect to the center of the cylinder. In all the cases a good agreement with previously published results [30] is attained. Additionally, Figs. 19 and 21 show good agreement with experimental results.

Fig. 22 shows the stream-wise velocity fluctuations along three transverse sections. Similarly, Fig. 23 shows the Reynolds shear stress along these transverse sections. In both the cases, the present results are in good agreement with the published results [30,44].

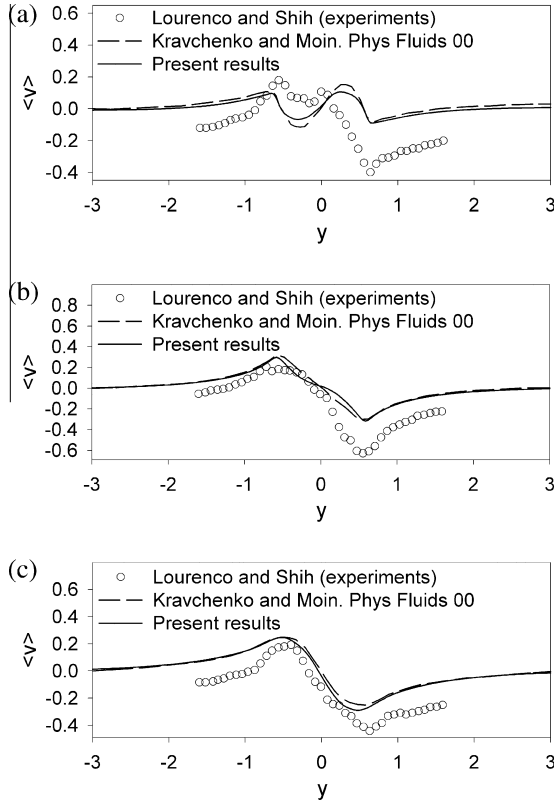

Fig. 20. Mean transversal velocity along: (a) $x = 1.06$, (b) $x = 1.54$ and (c) $x = 2.02$.

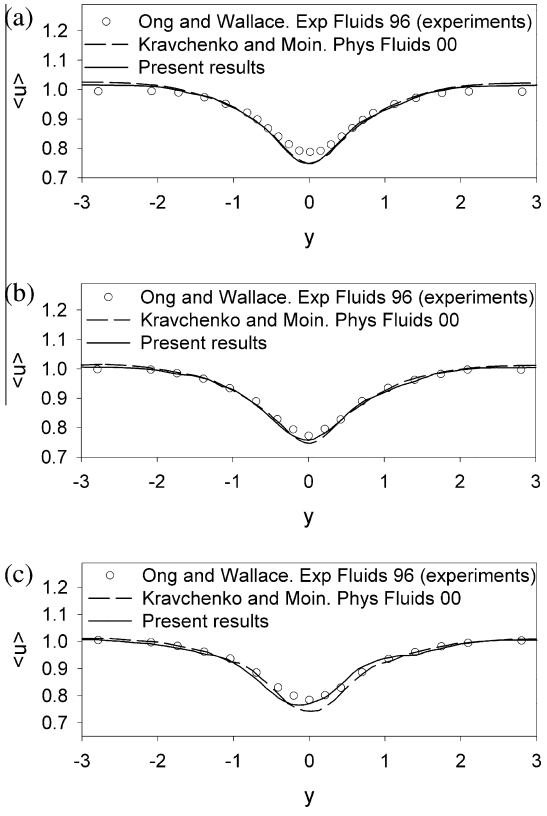

Fig. 21. Mean stream-wise velocity along: (a) $x = 6.00$, (b) $x = 7.00$ and (c) $x = 10.0$.

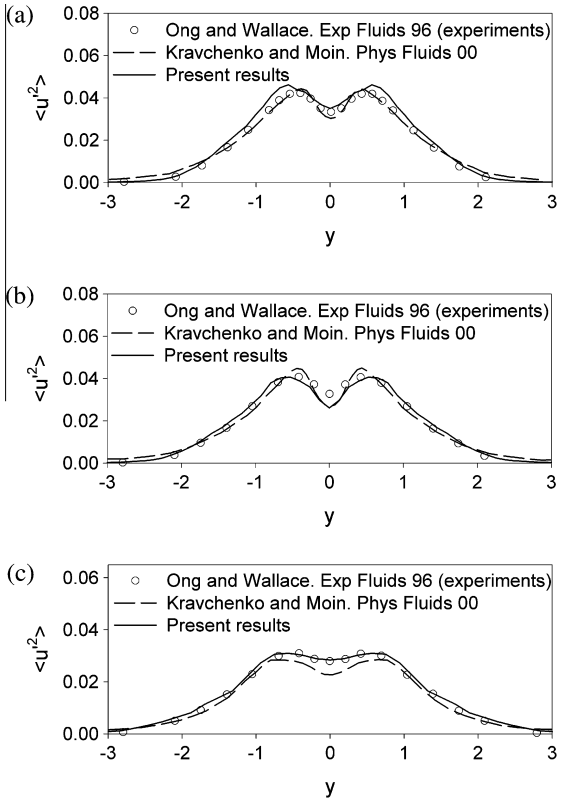

Fig. 22. Mean stream-wise velocity fluctuations along: (a) $x = 6.00$, (b) $x = 7.00$ and (c) $x = 10.0$.

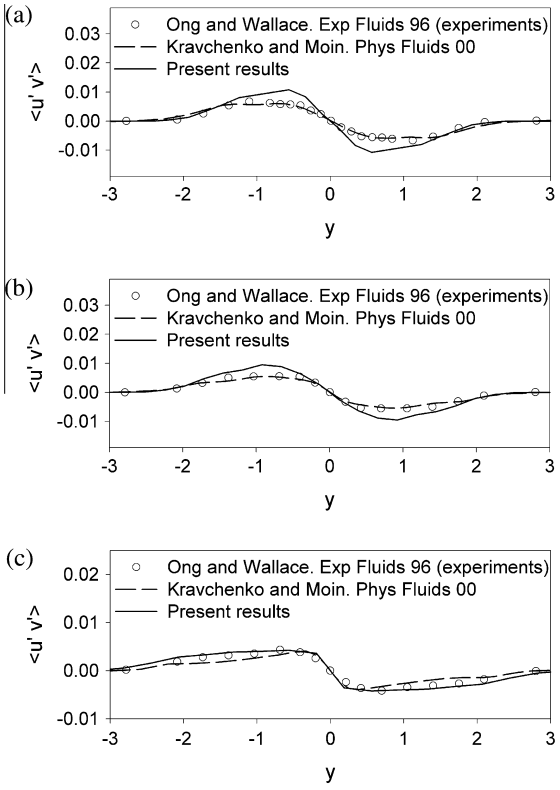

Fig. 23. Mean Reynolds shear stress along: (a) $x = 6.00$, (b) $x = 7.00$ and (c) $x = 10.0$.

5. Conclusion

We have presented a residual-based large eddy simulation model for incompressible turbulent flows. The proposed model differs from other VMS-based turbulence models in that a residual-free bubbles approach has been adopted to derive an analytical expression for the structure of the fine-scale variational operator $\boldsymbol{\tau}$. A direct treatment of the fine scale problem with bubble functions precludes the need for any modeling assumption on the form of the fine scales, and this constitutes the turbulence modeling paradigm within the VMS framework.

The proposed model has been implemented for the 8-node hexahedral elements, and numerically validated using three test cases of increasing degree of complexity: forced isotropic turbulence flow, turbulent channel flows at various *Re*, and turbulent flow around a cylinder. In all the cases, we have shown that our results compare very well with the results obtained via the traditional LES models, as well as with other VMS-based turbulence models.

The application of the bubble functions approach to the solution of the fine-scale problem offers several simplifying approximations for the representation of the fine scale fields. Employing the turbulent channel flow as a test case, we have investigated the effects of these modeling options. In particular, we have shown that an additive decomposition of the pressure field into coarse and fine scales provides a tighter control on the enforcement of the incompressibility constraint. On the other hand, if the fine-scale pressure is ignored, a general improvement in the mean flow statistics as well as in the fluctuations of the velocity components is observed. This improvement however comes at the cost of a loss in the local conservation property as the Reynolds number is increased. For the test cases employed here, the assumption of orthogonality of the fine-scales did not seem to affect the computed coarse scales in

any appreciable way. Furthermore, we showed that instead of projecting the full coarse-scale residual onto the fine-scale space to drive the fine-scale problem, employing an element-wise mean-value projection of the residual provides good accuracy in the computed coarse scales. Finally, we also confirm the phenomenon observed in [18,13] that if the dynamic effects of the fine-scale velocity are neglected, the stabilization feature of the formulation diminishes for very small time step sizes. However, if the fine-scales are considered to be time-dependent, the resolved coarse-scale features of the model stay uniformly stable and accurate even for very small time step sizes.

Acknowledgements

The authors thank Prof. T.J.R. Hughes for helpful discussions on VMS methods, and Prof. R.L. Taylor for discussions on implementation in the parallel version of FEAP. Mark Vanmoer of National Center for Supercomputing Applications generated some figures (Figs. 1, 6, 16). Computing resources were provided by the Teragrid Program under grant TG-DMS100004, and the Computational Science and Engineering program at the University of Illinois. During the course of this work, R. Calderer was supported by a fellowship from Caja Madrid Foundation. This support is gratefully acknowledged.

References

[1] I. Akkerman, Y. Bazilevs, V.M. Calo, T.J.R. Hughes, S. Hulshoff, The role of continuity in residual-based variational multiscale modeling of turbulence, Comput. Mech. 41 (2008) 371–378.
[2] J. Bardina, J.H. Ferziger, W.C. Reynolds, Improved sub-grid scale models for large eddy simulation, AIAA Paper No. 80-1357, 1980.
[3] Y. Bazilevs, V.M. Calo, J.A. Cottrell, T.J.R. Hughes, A. Reali, G. Scovazzi, Variational multiscale residual-based turbulence modeling for large eddy simulation of incompressible flows, Comput. Methods Appl. Mech. Engrg. 197 (2007) 173–201.
[4] Y. Bazilevs, C. Michler, V.M. Calo, T.J.R. Hughes, Isogeometric variational multiscale modeling of wall-bounded turbulent flows with weakly enforced boundary conditions on unstretched meshes, Comput. Methods Appl. Mech. Engrg. 199 (13–16) (2010) 780–790.
[5] F. Brezzi, L.P. Franca, T.J.R. Hughes, A. Russo, $b = \int g$, Comput. Methods Appl. Mech. Engrg. 145 (3–4) (1997) 329–339.
[6] F. Brezzi, D. Marini, A. Russo, Applications of the pseudo residual-free bubbles to the stabilization of convection–diffusion problems, Comput. Methods Appl. Mech. Engrg. 166 (1998) 51–63.
[7] R. Calderer, A. Masud, A multiscale stabilized formulation for incompressible fluids in moving boundaries, Comput. Mech. 46 (2010) 185–197.
[8] R. Codina, J. Principe, O. Guasch, S. Badia, Time dependent subscales in the stabilized finite element approximation of incompressible flow problems, Comput. Methods Appl. Mech. Engrg. 196 (21–24) (2007) 2413–2430.
[9] S.S. Collis, Monitoring unresolved scales in multiscale turbulence modeling, Phys. Fluids 13 (6) (2001) 1800–1806.
[10] T. Dubois, F. Jauberteau, R. Temam, Incremental unknowns, multilevel methods and the numerical simulation of turbulence, Comput. Methods Appl. Mech. Engrg. 159 (1–2) (1998) 123–189.
[11] C. Farhat, A. Rajasekharana, B. Koobus, A dynamic variational multiscale method for large eddy simulations on unstructured meshes, Comput. Methods Appl. Mech. Engrg. 195 (13–16) (2006) 1667–1691.
[12] L.P. Franca, C. Farhat, M. Lesoinne, A. Russo, Unusual stabilized finite element methods and residual free bubbles, Int. J. Numer. Methods Fluids 27 (2) (1998) 159–168.
[13] P. Gamnitzer, V. Gravemeier, W.A. Wall, Time-dependent subgrid scales in residual-based large eddy simulation of turbulent channel flow, Comput. Appl. Mech. Engrg. 199 (13–16) (2010) 819–827.
[14] M. Germano, U. Piomelli, P. Moin, W.H. Cabot, A dynamic subgrid-scale eddy viscosity model, Phys. Fluids A 3 (7) (1991) 1760–1765.
[15] V. Gravemeier, W.A. Wall, E. Ramm, Large eddy simulation of turbulent incompressible flows by a three-level finite element method, Int. J. Numer. Methods Fluids 48 (2005) 1067–1099.
[16] V. Gravemeier, The variational multiscale method for laminar and turbulent flow, Arch. Comput. Methods Engrg. State Art Rev. 13 (2006) 249–324.
[17] I. Harari, G. Hauke, Semidiscrete formulations for transient transport at small time steps, Int. J. Numer. Methods Fluids 54 (2007) 731–743.
[18] M.C. Hsu, Y. Bazilevs, V.M. Calo, T.E. Tezduyar, T.J.R. Hughes, Improving stability of stabilized and multiscale formulations in flow simulations at small time steps, Comput. Methods Appl. Mech. Engrg. 199 (13–16) (2010) 828–840.
[19] T.J.R. Hughes, M. Mallet, A new finite element formulation for computational fluid dynamics: III. The generalized streamline operator for multidimensional advective-diffusive systems, Comput. Methods Appl. Mech. Engrg. 58 (3) (1986) 305–328.
[20] T.J.R. Hughes, The Finite Element Method: Linear Static and Dynamic Finite Element Analysis, Dover Publications, Mineaola, NY, 1987.
[21] T.J.R. Hughes, L.P. Franca, A new finite element method for computational fluid dynamics: VII. The Stokes problem with various well-posed boundary conditions: symmetric formulations that converge for all velocity/pressure spaces, Comput. Methods Appl. Mech. Engrg. 65 (1987) 85–96.
[22] T.J.R. Hughes, Multiscale phenomena: Green's functions, the Dirichlet-to-Neumann formulation, subgrid scale models, bubbles and the origins of stabilized methods, Comput. Methods Appl. Mech. Engrg. 127 (1995) 387–401.
[23] T.J.R. Hughes, G.R. Feijoo, L. Mazzei, J.B. Quincy, The variational multiscale method – a paradigm for computational mechanics, Comput. Methods Appl. Mech. Engrg. 166 (1–2) (1998) 3–24.
[24] T.J.R. Hughes, L. Mazzei, K.E. Jansen, Large eddy simulation and the variational multiscale method, Comput. Visual. Sci. 3 (1–2) (2000) 47–59.
[25] T.J.R. Hughes, A.A. Oberai, L. Mazzei, Large eddy simulation of turbulent channel flows by the variational multiscale method, Phys. Fluids 13 (6) (2001) 1784–1799.
[26] K.E. Jansen, A stabilized finite element method for computing turbulence, Comput. Methods Appl. Mech. Engrg. 174 (3–4) (1999) 299–317.
[27] K.E. Jansen, C.H. Whiting, G.M. Hulbert, A generalized alpha method for integrating the Navier–Stokes equations with a stabilized finite element method, Comput. Methods Appl. Mech. Engrg. 190 (2000) 305–319.
[28] R. Khurram, A. Masud, A multiscale/stabilized formulation of the incompressible Navier–Stokes equations for moving boundary flows and fluid-structure interaction, Comput. Mech. 38 (4–5) (2006) 403–416.
[29] B. Koobus, C. Farhat, A variational multiscale method for the large eddy simulation of compressible turbulent flows on unstructured meshes – application to vortex shedding, Comput. Methods Appl. Mech. Engrg. 193 (2004) 1367–1383.
[30] A.G. Kravchenko, P. Moin, Numerical studies of flow over a circular cylinder at Re_D = 3900, Phys. Fluids 12 (2) (2000) 403–417.
[31] D.K. Lilly, A proposed modification of the Germano subgrid-scale closure method, Phys. Fluids A 4 (3) (1992) 633–635.
[32] K. Mahesh, G. Constantinescu, P. Moin, A numerical method for large-eddy simulation in complex geometries, J. Comput. Phys. 197 (1) (2004) 215–240.
[33] A. Masud, R. Khurram, A multiscale/stabilized finite element method for the advection–diffusion equation, Comput. Methods Appl. Mech. Engrg. 193 (2004) 1997–2018.
[34] A. Masud, K. Xia, A stabilized mixed finite element method for nearly incompressible elasticity, J. Appl. Mech. 72 (2005) 711–720.
[35] A. Masud, R. Khurram, A multiscale finite element method for the incompressible Navier–Stokes equations, Comput. Methods Appl. Mech. Engrg. 195 (2006) 1750–1777.
[36] A. Masud, A stabilized mixed finite element method for Darcy–Stokes flow, Int. J. Numer. Methods Fluids 54 (3) (2007) 57–73.
[37] A. Masud, J. Kwack, A stabilized mixed finite element method for the first-order form of convection-diffusion equation, Int. J. Numer. Methods Fluids 57 (2008) 1321–1348.
[38] A. Masud, L.P. Franca, A hierarchical multiscale framework for problems with multiscale source terms, Comput. Methods Appl. Mech. Engrg. 197 (2008) 2692–2700.
[39] A. Masud, R. Calderer, A variational multiscale stabilized formulation for the incompressible Navier–Stokes equations, Comput. Mech. 44 (2009) 145–160.
[40] P. Moin, Advances in large eddy simulation methodology for complex flows, Int. J. Heat Fluid Flow 23 (5) (2002) 710–720.
[41] R. Moser, J. Kim, R. Mansour, DNS of turbulent channel flow up to Re = 590, Phys. Fluids 11 (1999) 943–945.
[42] A. Novikov, D. Bodony, A multiscale, asymptotic model for the subgrid scale stresses in the large-eddy simulation of an incompressible fluid, in: Annual Research Briefs, Center for Turbulence Research, Stanford, CA, 2005, pp. 195–210.
[43] A.A. Oberai, T.J.R. Hughes, The variational multiscale formulation of LES: channel flow at Re_τ = 590, in: 40th AIAA Annual Meeting, Reno, NV, AIAA 2002-1056, 2002.
[44] L. Ong, J. Wallace, The velocity field of the turbulent very near wake of a circular cylinder, Exp. Fluids (1996).
[45] S.B. Pope, Turbulent Flows, Cambridge University Press, Cambridge, 2000.
[46] A. Rajasekharan, C. Farhat, C. Bou-Mosleh, Application of a dynamic variational multiscale method to the LES of separated turbulent flows, in: 45th AIAA Aerospace Sciences Meeting and Exhibit, Reno, NV, 2007.
[47] A. Rajasekharan, C. Farhat, Applications of a variational multiscale method for large eddy simulation of turbulent flows on moving/deforming unstructured grids, Finite Elem. Anal. Des. 45 (2009) 272–279.
[48] J. Smagorinsky, General circulation experiments with the primitive equations. I. The basic experiment, Mon. Weather Rev. 91 (1963) 99–164.
[49] A.E. Tejada-Martínez, K.E. Jansen, A parameter-free dynamic subgrid-scale model for large-eddy simulation, Comput. Methods Appl. Mech. Engrg. 195 (23–24) (2006) 2919–2938.
[50] J. Yang, E. Balaras, An embedded-boundary formulation for large-eddy simulation of turbulent flows interacting with moving boundaries, J. Comput. Phys. 215 (2006) 12–40.